JCB Journal of Cell Biology

ARTICLE

Wnt signaling establishes the microtubule polarity in neurons through regulation of Kinesin-13

Dharmendra Puri[1], Keerthana Ponniah[1], Kasturi Biswas[1], Atrayee Basu[1], Swagata Dey[1], Erik A. Lundquist[2], and Anindya Ghosh-Roy[1]

Neuronal polarization is facilitated by the formation of axons with parallel arrays of plus-end-out and dendrites with the nonuniform orientation of microtubules. In *C. elegans*, the posterior lateral microtubule (PLM) neuron is bipolar with its two processes growing along the anterior–posterior axis under the guidance of Wnt signaling. Here we found that loss of the Kinesin-13 family microtubule-depolymerizing enzyme KLP-7 led to the ectopic extension of axon-like processes from the PLM cell body. Live imaging of the microtubules and axonal transport revealed mixed polarity of the microtubules in the short posterior process, which is dependent on both KLP-7 and the minus-end binding protein PTRN-1. KLP-7 is positively regulated in the posterior process by planar cell polarity components of Wnt involving *rho-1/rock* to induce mixed polarity of microtubules, whereas it is negatively regulated in the anterior process by the *unc-73/ced-10* cascade to establish a uniform microtubule polarity. Our work elucidates how evolutionarily conserved Wnt signaling establishes the microtubule polarity in neurons through Kinesin-13.

Introduction

Neurons are polarized cells compartmentalized into long axons and relatively shorter dendrites. During the development of the neural circuit, axons are specified by both extrinsic cues and intrinsic programs (Yogev and Shen, 2017). The microtubule cytoskeleton, assembled from α and β tubulin dimers, is the building block of axons and dendrites (Komarova et al., 2002; Kapitein and Hoogenraad, 2015; van Beuningen and Hoogenraad, 2016). Microtubule polymers are inherently dynamic in the cell, undergoing polymerization and depolymerization (Mitchison and Kirschner, 1984). During the initial stages of polarization, microtubules are stabilized in one of the nascent neurites fated to become an axon (Witte et al., 2008). However, shorter neurites have microtubules of opposing polarity during the initial stages of polarization, which remain unchanged even in the mature dendrites (Yau et al., 2016; Baas et al., 1988).

How microtubule dynamics are regulated during and after neuronal polarization is not understood in great detail. The collapsin response mediator protein CRMP/UNC-33 is important for microtubule assembly during the establishment of neuronal polarity (Arimura et al., 2004; Yoshimura et al., 2005; Maniar et al., 2012). The microtubule plus- and minus-end binding proteins are also important in this process (Leterrier et al., 2011; Yau et al., 2014). In the axon, TRIM46 promotes the cross-linking of microtubules to enable the formation of a microtubule array with plus-end-out polarity (van Beuningen et al., 2015). Formation of parallel arrays of microtubules stimulates directional vesicular trafficking into the axons, which helps the growth of axons toward the target tissues (Yogev et al., 2016; Nakata and Hirokawa, 2003; Rolls, 2011; Tas et al., 2017). A question of fundamental interest is how microtubule polarity in axons and dendrites is established and maintained. Similarly, it has become imperative to understand how the extrinsic cues regulate microtubule dynamics during neuronal polarization.

Caenorhabditis elegans mechanosensory neurons, responsible for gentle touch sensation, have been used extensively to understand the regulation of the microtubule cytoskeleton (Lumpkin et al., 2010; Bounoutas and Chalfie, 2007; Chalfie and Thomson, 1982). Both the anterior lateral microtubule (ALM) and posterior lateral microtubule (PLM) touch neurons bear a long anterior axon containing 15 microtubule protofilaments (Chalfie and Thomson, 1982) and a shorter posterior neurite. Previous reports have documented mutations in tubulin subunits, which affect the development of touch neurons (Lockhead et al., 2016; Zheng et al., 2017; Cueva et al., 2012). The polarity of these neurons is established by the Wnt signaling (Hilliard and Bargmann, 2006; Prasad and Clark, 2006; Zheng et al., 2015; Ackley, 2014). However, it is unclear how Wnt signaling regulates the microtubule dynamics to establish the polarity of the touch neurons.

In this study, we found that the Kinesin-13 family microtubule-depolymerizing factor kinesin-like protein 7 (KLP-7) is important for the proper polarization of touch neurons. Using live imaging

[1]Department of Cellular and Molecular Neuroscience, National Brain Research Centre, Manesar, Gurgaon, Haryana, India; [2]Department of Molecular Biosciences, University of Kansas, Lawrence, KS.

Correspondence to Anindya Ghosh-Roy: anindya@nbrc.ac.in; K. Biswas's present address is Department of Neurobiology, University of Massachusetts Medical School, Worcester, MA.

https://doi.org/10.1083/jcb.202005080

of plus- and minus-end binding proteins (Ghosh-Roy et al., 2012; Akhmanova and Hoogenraad, 2015), we found that the microtubules in the posterior process are oriented in mixed polarity. The minus-end binding protein Patronin-1 (PTRN-1) is required for maintaining the minus-end-out population of microtubules in the posterior process. The loss of KLP-7 makes the microtubules unipolar in the posterior process and promotes bidirectional transport, leading to its overextension. Conversely, overexpression of KLP-7 makes the microtubules oriented randomly even in the anterior process, leading to its shortening. This process works downstream to Wnt signaling because loss of *klp-7* suppressed the reversal of microtubule polarity caused by loss of Wnt ligand LIN-44 or its receptor LIN-17. Our data suggest that downstream noncanonical components of the Wnt signaling positively regulate KLP-7 in the posterior process and negatively in the anterior process for proper organization of the microtubule cytoskeleton.

Results

Loss of Kinesin-13 family microtubule-depolymerizing enzyme KLP-7 leads to the formation of multiple axon-like projections in touch neurons

In *C. elegans*, there are six mechanosensory neurons that are responsible for sensing the gentle touch (Bounoutas and Chalfie, 2007). Among these, the ALM neuron and PLM neuron grow their axons laterally toward the anterior side and connect to their respective post-synaptic neurons through a ventral synaptic branch (white arrows, Fig. 1 A). Additionally, the PLM neuron has a relatively shorter posterior process (double-sided arrow, Fig. 1 A), whose function is still unclear. In the anterior process of the PLM neuron, synaptic protein GFP::RAB-3 gets transported toward the ventral nerve cord, where it makes en passant synapses to the AVA neuron (white arrowheads, Fig. 1 C; Bounoutas and Chalfie, 2007). Compared with the anterior process, the posterior process contained fewer GFP::RAB-3 punctae (green arrowheads, Fig. 1 C).

Since the regulation of microtubule dynamics influences neuronal polarity (Witte et al., 2008), we tested various mutants with perturbed microtubule dynamics (Table S1) for the possible phenotype in touch neuron polarity. Among the mutants we tested, loss of Kinesin-13 family microtubule-depolymerizing factor KLP-7 caused a strong morphological phenotype in ALM and PLM neurons (Table S1; Fig. 1 A), which was briefly stated in a previous report (Ghosh-Roy et al., 2012). In addition to the anterior axon, which connects to the nerve ring (yellow arrowhead, Fig. 1 A), the ALM neuron also had a long posterior process (orange arrow, Fig. 1, A and C) in both *tm2143* (820-bp deletion) and a CRISPR-induced allele *shr3* (Fig. 1 B). We also noticed an overgrowth phenotype of the posterior process in the PLM neuron (white double-sided arrow, Fig. 1 A). The WT worms phenocopied the defect noticed in *klp-7(0)* upon Taxol treatment (Fig. S1, A–C) that stabilizes the microtubule (Schiff et al., 1979). Conversely, when the *klp-7(0)* worms were grown in plates containing colchicine, the ectopic growth was significantly reduced in the ALM neuron (Fig. 1 B). We found that the presynaptic reporters GFP::RAB-3 (green arrowheads, Fig. 1, C and D) and TagRFP::ELKS-1 (magenta arrowheads, Fig. S1 E) were visible in the ectopic processes as frequently as those in the anterior process of the *klp-7* mutant.

The phenotype of ALM was significantly rescued when a WT copy of *klp-7* was expressed under the control of either a touch neuron *(mec-4)* or a neuronal (*unc-86*) promoter (Fig. 1 B). However, the *klp-7b* isoform was better able to rescue than the *klp-7a* isoform (Fig. 1 B). Conversely, overexpression of *klp-7* in a WT background reduced the lengths of both the anterior and posterior processes significantly (Fig. 1, A, E, and F). A similar effect was seen in the worms upon colchicine treatment (Fig. S1, C and D). Altogether, these data suggested that in the touch neurons, the activity of KLP-7 as a microtubule-depolymerizing enzyme is important to restrain the unwanted growth from the cell body during neuronal polarization. This is further supported by the enrichment of KLP-7 in the touch neurons, as observed (arrows, Fig. 1 G) by both *Pklp-7*–KLP-7::GFP reporter (Sarov et al., 2012) and anti–KLP-7 immunostaining (Fig. S1 F, arrows).

Similarly, in PVD neurons as well, we observed ectopic neurites in *klp-7(0)* (arrow, Fig. S1 G). We noticed that synaptic protein RAB-3 was mislocalized to the dendrites in *klp-7(0)* (magenta arrowheads, Fig. S1, G and H). This indicated that dendritic processes can take on an axon-like identity in the absence of KLP-7, further supporting the role of KLP-7 in neuronal polarity.

KLP-7 is necessary and sufficient to maintain dynamic microtubules in the posterior process of the PLM

To understand how microtubules are affected in *klp-7(0)*, we imaged the growing microtubules in the PLM (Video 1) using the end binding protein 2 (EBP-2)::GFP reporter (Ghosh-Roy et al., 2012). We determined the direction of microtubule growth from the slopes of the diagonal tracks in the kymographs (Fig. 2 B) from the regions of interest (ROIs) in the anterior and posterior processes (Fig. 2 A). In the WT background, the anterior process had the majority of the EBP-2 movements away from the cell body (plus-end-out, green trace denoted as P), while in the posterior process, we noticed comparable movements toward (minus-end-out, magenta trace denoted as M) and away from the cell body (Fig. 2 B). We quantified the fractions of microtubule tracks with plus-end-out or minus-end-out orientation (Fig. 2 C). In the anterior process, 88% of the microtubules had plus-end-out orientation (Fig. 2 C). In the posterior process, the percentages of plus-end-out and minus-end-out microtubules were ∼50% each (Fig. 2 C). In addition, we noticed that the overall number of tracks was higher in the posterior process (Table S2). However, growth length and growth duration of these tracks were significantly smaller than in the anterior process (Fig. 2, E and F). This indicated an increased microtubule dynamics in the posterior process. In *klp-7(0)* (Video 1), we observed relatively fewer EBP-2 tracks in the kymographs (Fig. 2 B; Table S2) with longer growth lengths (Fig. 2 E), indicating an increased stability of microtubules. In addition, the microtubules in the posterior process became uniformly oriented (Fig. 2 B) with either plus-end-out (class 1; Fig. 2 B) or minus-end-out (class 2; Fig. 2 B) orientation, with a high variation in the fraction polarity values (Fig. 2 C, red arrowheads representing segregation of values). The frequency distribution of microtubule

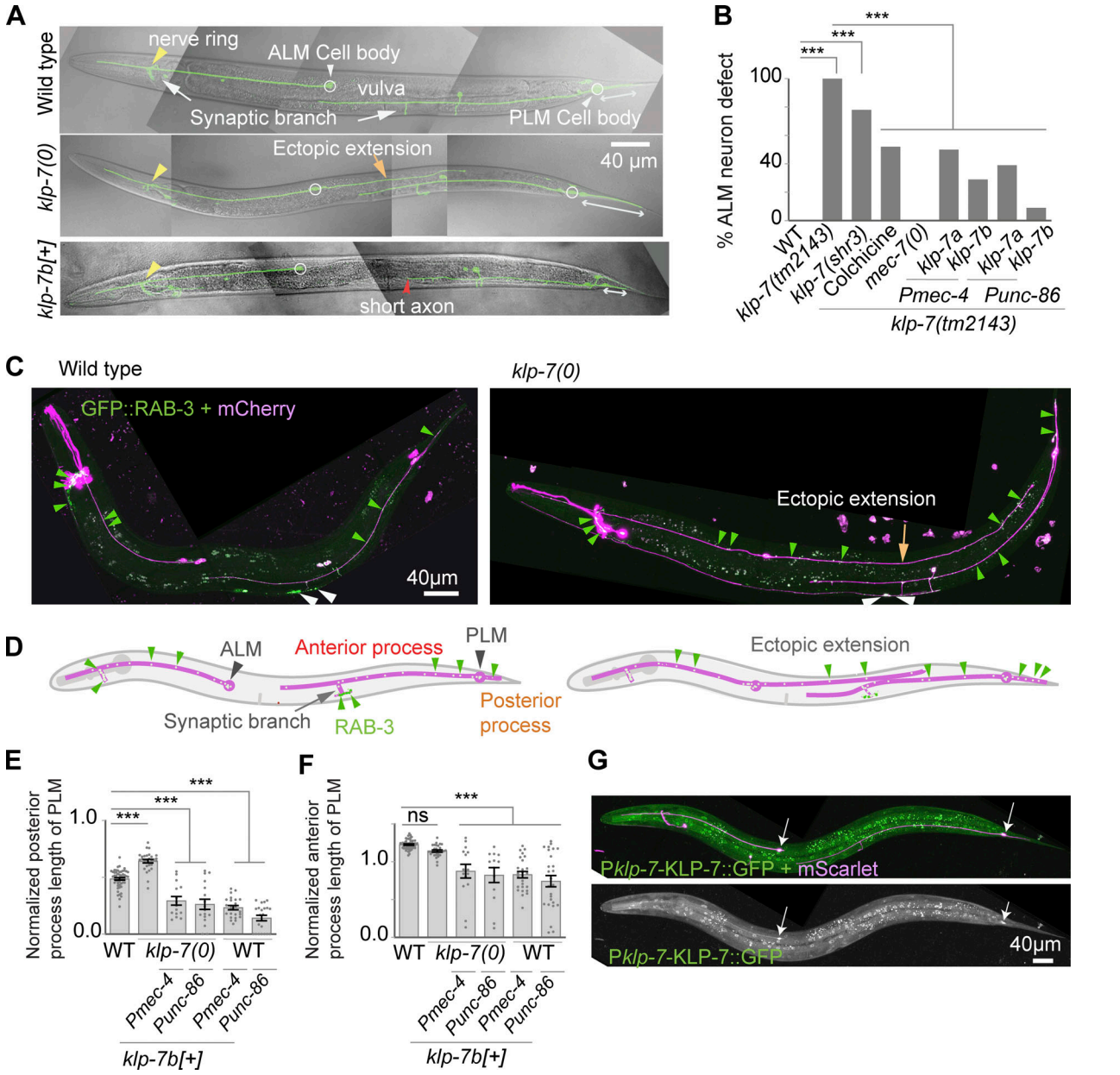

Figure 1. **KLP-7 restricts neurite growth in TRNs. (A)** Confocal images of ALM and PLM neurons expressing *Pmec-7*::GFP (*muIs32*) in WT, in *klp-7(tm2143)*, and in WT background expressing *Pmec-4*::*klp-7b* (*shrEx93*). Yellow arrowheads and white arrows indicate the position of the nerve ring and synaptic branch, respectively. In *klp-7(tm2143)*, the posterior process of the ALM shows ectopic growth (orange arrow), while the PLM posterior process is extended moderately (double-sided arrow). In the *Pmec-4*::*klp-7b[+]* background, often the anterior process of the PLM is terminated prematurely (red arrowhead). **(B)** Quantification of ectopic extension in the ALM in *klp-7* mutants. N = 4–6 independent replicates; *n* (number of neurons) = 80–194. **(C and D)** Confocal images and illustration of the *Pmec-7*::GFP::RAB-3 (*jsIs821*) and *Pmec-4*-mCherry (*tbIs222*) reporters in the WT and *klp-7(0)* backgrounds. Yellow arrow indicates the ectopic process in ALM. The green arrowheads indicate GFP::RAB-3 punctae along the processes of PLM and ALM neurons. The white arrowheads indicate the GFP::RAB-3 enrichment at the synaptic region of PLM. **(E and F)** The normalized length of PLM posterior and anterior processes due to either loss or overexpression of *klp-7*. Normalized length = (actual length/distance between cell body and vulva for anterior process or distance between cell body to tail tip for posterior process). N = 3–6 independent replicates; *n* (number of neurons) = 15–55. **(G)** Confocal image of TRNs (arrows) in worms expressing *Pklp-7*-KLP-7::GFP (*ddIs145*) in *Pmec-4-mScarlet* (*shrEx143*) background. For B, ***, P < 0.001; Fisher's exact test. For E and F, ***, P < 0.001; ANOVA with Tukey's multiple comparison test. Error bars represent SEM.

polarity in PLM processes (Fig. S2, A–D) made this dispersion more evident. In the WT background, the fraction of microtubules with plus-end-out polarity showed a normal distribution with a modal value of 0.5 (asterisk, Fig. S2 C) for the posterior processes, whereas in *klp-7(0)*, there were two-mode values of 1 and 0. We classified processes with a fraction polarity value of 0.8 or more as unipolar (gray shaded box, Fig. S2, A–D). Anything below 0.8 is categorized as a process with mixed microtubule polarity. On the basis of this criterion, in WT background, 83% of the anterior and 16% of the posterior processes were unipolar

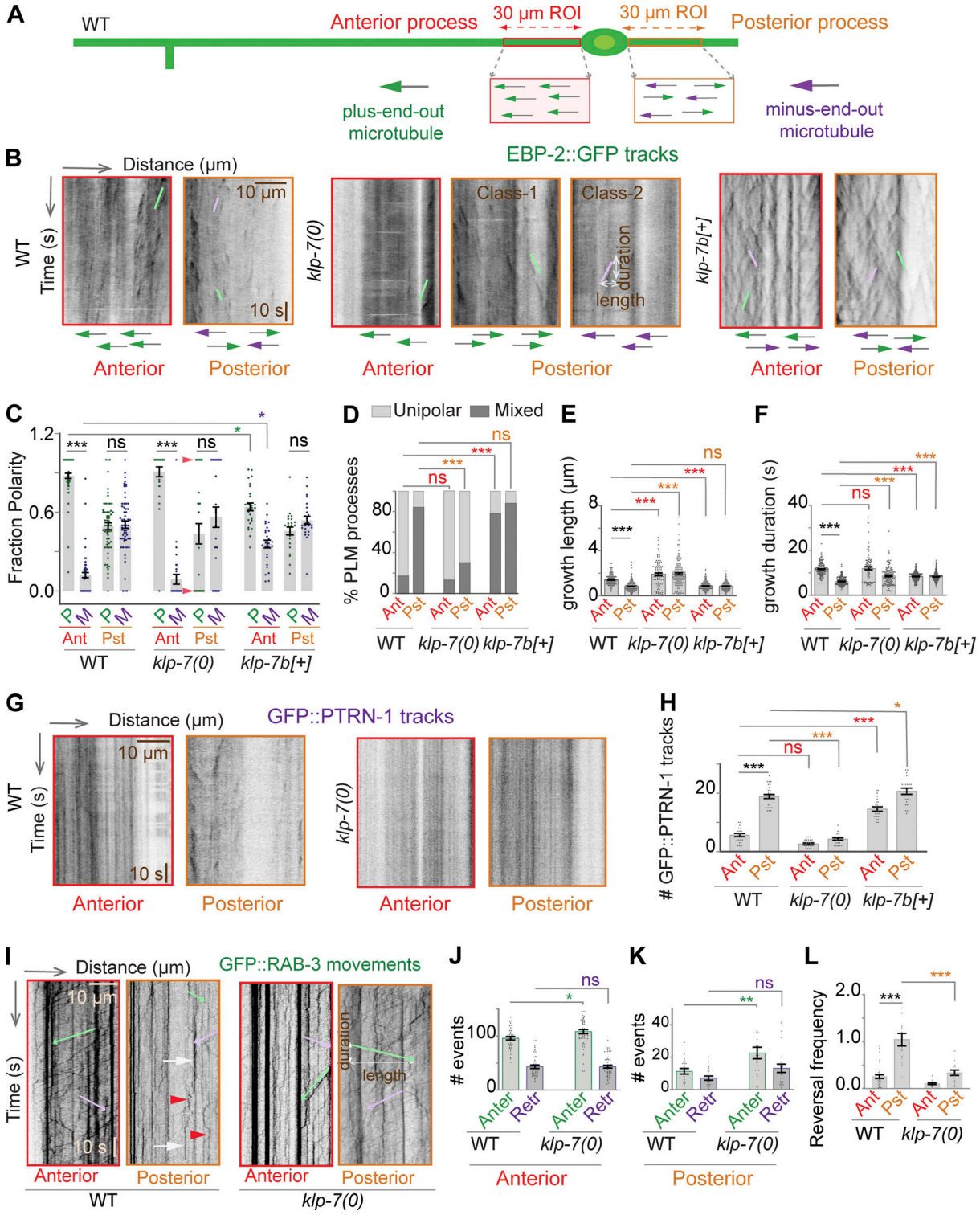

Figure 2. **KLP-7 is necessary and sufficient to maintain dynamic microtubules in the PLM neuron. (A)** Illustration of the PLM neuron and kymographs of EBP-2::GFP reporter. Red and orange ROIs were used for the analysis of time-lapse movies (Video 1) of the *Pmec-4*::EBP-2::GFP (*juIs338*) reporter. Green and magenta arrows represent the microtubules of plus-end-out and minus-end-out polarity, respectively. **(B)** Representative kymographs (inverted grayscale) of EBP-2::GFP dynamics (Video 1) obtained from the ROIs in A in WT, *klp-7(0)*, and *Pmec-4*::KLP-7B (*shrEx95*)[+]. The green and magenta traces represent microtubule growth events away from the cell body/plus-end-out and toward the cell body/minus-end-out, respectively. In all kymographs, the length (x axis) and time (y axis) scales are 10 µm and 10 s, respectively. **(C)** The histogram shows the fraction of microtubules with plus-end-out (P) or minus-end-out (M) polarity. The red arrowheads represent the segregation of fraction polarity values in the posterior process into 1 and 0 in the *klp-7* mutant. N = 3–8 independent replicates, *n* (number of neurons) = 28–63. Ant, anterior; Pst, posterior. **(D)** The percentage of PLM processes with microtubules oriented in either unipolar or mixed manner. N = 3–8; *n* = 28–63. **(E and F)** Growth length and duration of the EBP-2::GFP tracks were measured from net pixel shift in the x and y axes, respectively, as indicated by the double-headed arrows in B. N = 3–4 independent replicates; *n* (number of EBP-2 tracks) = 92–628. **(G)** Kymographs of

Pmec-4-GFP::PTRN-1 (*juEx6455*) reporter in WT and *klp-7(0)*. **(H)** The number of growing minus ends in PLM processes as obtained from G. *n* = 3–5 independent replicates, *n* (number of neurons) = 16–25. **(I)** Kymographs obtained from the time-lapse movie (Video 2) of the *Pmec-7*-GFP::RAB-3 (*jsIs821*) reporter show the events of anterograde (green arrow trace) and retrograde (magenta arrow trace) movement. The white arrows show the stationary particles, whereas the red arrowheads represent RAB-3 particles frequently switching direction. **(J and K)** Quantification of the anterograde (Anter) and retrograde (Retr) movement events of GFP::RAB-3 particles obtained from I. N = 3–8 independent replicates; *n* (number of neurons) = 31–56. **(L)** Reversal frequency as measured by the number of reversal events divided by the total number of events. N = 3–5 independent replicates; *n* = 17–40 (number of neurons). For C, E, F, H, and J–L, *, P < 0.05; **, P < 0.01; ***, P < 0.001; ANOVA with Tukey's multiple comparison test. For D, **, P < 0.01; Fisher's exact test. Error bars represent SEM.

(Fig. 2 D). However, in *klp-7(0)*, the unipolar posterior processes increased to 70%. Conversely, when the WT copy of *klp-7* was overexpressed, the number of EBP-2 tracks increased in both the processes (Fig. 2 B; Table S2), indicating an increased instability. Similarly, in the anterior process, the microtubules become randomly oriented (Fig. 2 B). Approximately 78% of the anterior processes were with mixed microtubule orientation (Fig. 2 D). This indicated that KLP-7 is sufficient to induce mixed polarity of microtubules in the PLM neuron. Imaging of the reporter for the minus-end binding protein calmodulin-regulated spectrin-associated protein 2 (CAMSAP2)/PTRN-1 (Akhmanova and Hoogenraad, 2015; Chuang et al., 2014) revealed that there is a small population of growing minus ends in the posterior process, which was missing in *klp-7(0)* (Fig. 2, G and H). The total count of GFP::PTRN-1 punctae was also significantly reduced in the posterior process in *klp-7(0)* (Fig. S2, E and F). Overexpression of KLP-7 increased the number of growing minus ends in both the processes (Fig. 2 H). This indicated that KLP-7 is required to maintain a dynamic population of minus ends in the posterior process.

Imaging of the GFP::RAB-3 reporter (Mondal et al., 2011) in the similar ROIs (Fig. 2 A; and Video 2) revealed that the number of anterograde (green arrow, Fig. 2 I) and retrograde (blue arrow, Fig. 2 I) transport events in the anterior process was higher (Fig. 2, I–K). Most of the particles in the posterior process were static (white arrows, Fig. 2 I), with residual movement showing a frequent reversal in direction (red arrowheads, Fig. 2, I and L). In both the processes, there was a significant increase in the anterograde transport events in *klp-7(0)* (Fig. 2, I–K; and Video 2). The length and duration of the transport events were also significantly higher in *klp-7(0)* (Fig. S2, G and H), along with reduced reversal frequency (Fig. 2 L). Taken together, this indicated that in the absence of KLP-7, microtubules tend to be stable and unipolar, stimulating the transport of axonal cargo in all the neurites.

KLP-7 and PTRN-1 together establish mixed polarity orientation of microtubules in the posterior process

We hypothesized that the minus-end-out population in the posterior process of the PLM could be maintained by the activity of the minus-end binding protein PTRN-1 (Akhmanova and Hoogenraad, 2015; Feng et al., 2019). Consistently, the microtubules in the posterior process predominantly adopt plus-end-out polarity in both *ptrn-1(0)* single mutant and *klp-7(0);ptrn-1(0)* (Fig. 3, B–D). An overexpression of *ptrn-1* makes the microtubules in the posterior process mainly of minus-end-out polarity (Fig. 3, B and C). However, neither the loss nor the overexpression of *ptrn-1* could change the polarity of the microtubules in the anterior process (Fig. 3, B–D).

It is not clear why, in the posterior process, the microtubules are exclusively either plus-end-out or minus-end-out in *klp-7(0)*. There could be one or a few microtubule nucleating centers in the posterior process of the PLM, as reported in dendrite-like processes (Liang et al., 2020; Harterink et al., 2018). During the early stages of development, the nucleating center could be captured in random orientation in the posterior process, which might generate either plus-end-out or minus-end-out microtubules. In the presence of active KLP-7, microtubules will assume mixed orientation. We observed only one puncta of centrosomal marker GIP-2 (Liang et al., 2020) in the posterior process at the L1 as well as the L4 stage (Fig. 3 E). Consistently, we found that at the L1 larval stage, there were few EBP-2 tracks in the posterior process (Fig. 3 F and Table S2), exclusively with either plus-end-out or minus-end-out polarity (Fig. 3, F and G, red arrows). From the L2 stage, we noticed a posterior process with mixed microtubule polarity, with fraction polarity values centering on 0.5 (Fig. 3, G and H). In the L3 stage, microtubule polarity was completely mixed (Fig. 3, F–H), whereas in *klp-7(0)*, the distribution of the posterior process in terms of microtubule arrangement remained the same, as seen in the L1 stage (Fig. 3, F–H). This also strengthened the points that KLP-7 activity in the early stages of development induces mixed polarity of microtubules in the posterior process and that the minus-end-out population would be maintained by PTRN-1.

In the absence of Wnt signaling, microtubule polarity in the PLM is reversed

Length of the anterior and posterior processes of the PLM neuron is optimized by a high concentration of Wnt ligand LIN-44 and its receptor LIN-17 in the tail region of the worm. In the absence of either *lin-17* or *lin-44*, the polarity of the PLM neuron is reversed, with its small posterior process growing longer and making ectopic synapses in the tail region (Hilliard and Bargmann, 2006; Prasad and Clark, 2006; Fig. 4 A). In *lin-17(0)*, analysis of the EBP-2::GFP movies showed that the microtubule orientation in the anterior process became mixed (Video 1; and Fig. 4, B and C), whereas in the posterior process, ∼89% of tracks were oriented in plus-end-out manner, and the majority of these processes were unipolar (Fig. 4 D). The number of tracks in the anterior process was relatively higher in this mutant (Table S2). Moreover, the growth length and duration of the microtubules were significantly smaller in the anterior process in *lin-17(0)* (Fig. 4, E and F). This indicated that microtubules are relatively dynamic in the anterior process, which was also indicated by an increased number of growing minus ends in the anterior process in the *lin-17(0)* background (Fig. 4, G and H). A similar effect on microtubule orientation and dynamics was also observed in *lin-44(0)* (Fig. 4, C–F).

This was further reinforced by the imaging of GFP::RAB-3 in *lin-17(0)*, which revealed a drastic reduction in both the anterograde

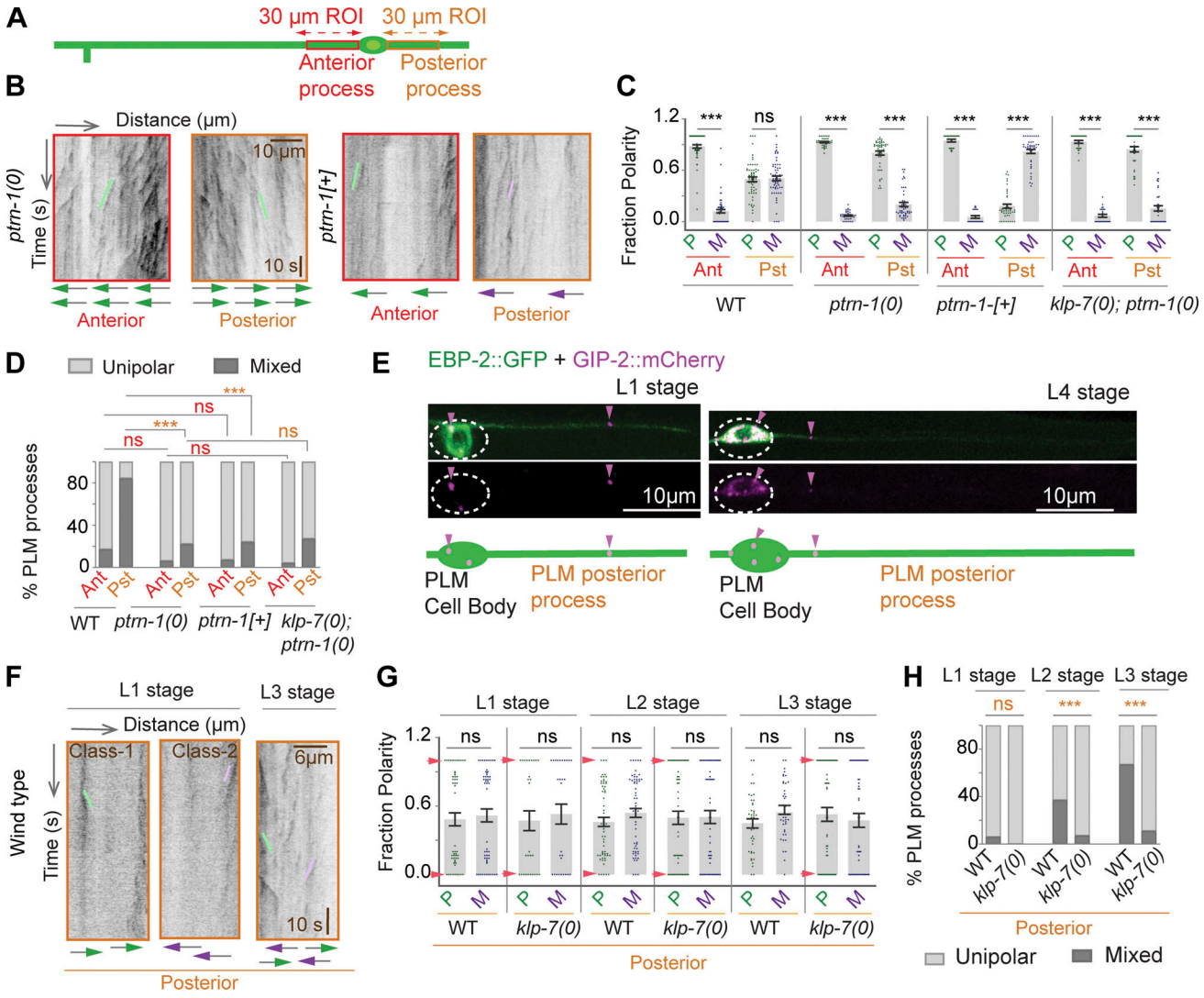

Figure 3. **KLP-7 and PTRN-1 together maintain the mixed polarity state of microtubules in the posterior process. (A and B)** The analysis of EBP-2::GFP dynamics in *ptrn-1-(0)* and *ptrn-1 (juEx5550)*[+]. The green and magenta traces represent microtubules of plus-end-out and minus-end-out polarity, respectively. **(C)** The histogram shows the fraction of plus-end-out (P) and minus-end-out (M) microtubules as obtained from the kymographs shown in B. Ant, anterior; Pst, posterior. **(D)** The percentage of PLM processes with microtubules oriented in either a unipolar or mixed manner as derived from C. For C and D, N = 3–5 independent replicates; *n* (number of neurons) = 23–63. **(E)** The punctae (magenta arrowheads) of centrosomal reporter P*mec-4*::GIP-2::mCherry (*shrEx413*) in the cell body and posterior process of the PLM neuron. **(F)** Kymographs of EBP-2::GFP movies in the posterior process from early developmental stage L1 to L3. **(G)** The distribution of plus-end-out and minus-end-out microtubule populations in the posterior process as obtained from F. The red arrowheads represent the segregation of fraction polarity values into 1 and 0. **(H)** The fraction of unipolar versus mixed-orientation posterior processes as obtained from F and G. N = 3–4 independent replicates; *n* (number of neurons) = 28–60. For C and G, ***, P < 0.001; ANOVA with Tukey's multiple comparison test. For D and H, ***, P < 0.001; Fisher's exact test. Error bars represent SEM.

and retrograde movements in the anterior process (Video 2; and Fig. 4, I–K). Instead, the posterior process in the *lin-17(0)* background showed considerable movement in both directions with an anterograde bias (Video 2; and Fig. 4, I and K). Overall, these results showed that both microtubule polarity and axonal transport are reversed in the absence of Wnt signaling.

Loss of *klp-7* restores the polarity switch of microtubules in *Wnt* mutants

We hypothesized that the increased microtubule instability and shortening of the anterior process in *Wnt* mutants is due to the abnormal activation of KLP-7 in the anterior process. We found that loss of *klp-7* can significantly suppress the neuronal polarity reversal phenotype in both *lin-17(0)* and *lin-44(0)* backgrounds (Fig. 5, A and B). A similar trend was also noticed in Dishevelled mutant *dsh-1(0);mig-5(0)* acting downstream of LIN-17 (Zheng et al., 2015; Fig. 5 B). However, neither the loss nor the overexpression of *ptrn-1* could change the phenotype in the *lin-17(0)* background (Fig. 5 B). This indicated that PTRN-1–mediated microtubule stability is not sufficient to reset the defects in *Wnt* mutants.

Imaging of the EBP-2::GFP reporter revealed that the microtubule polarity defect was also significantly rectified in the

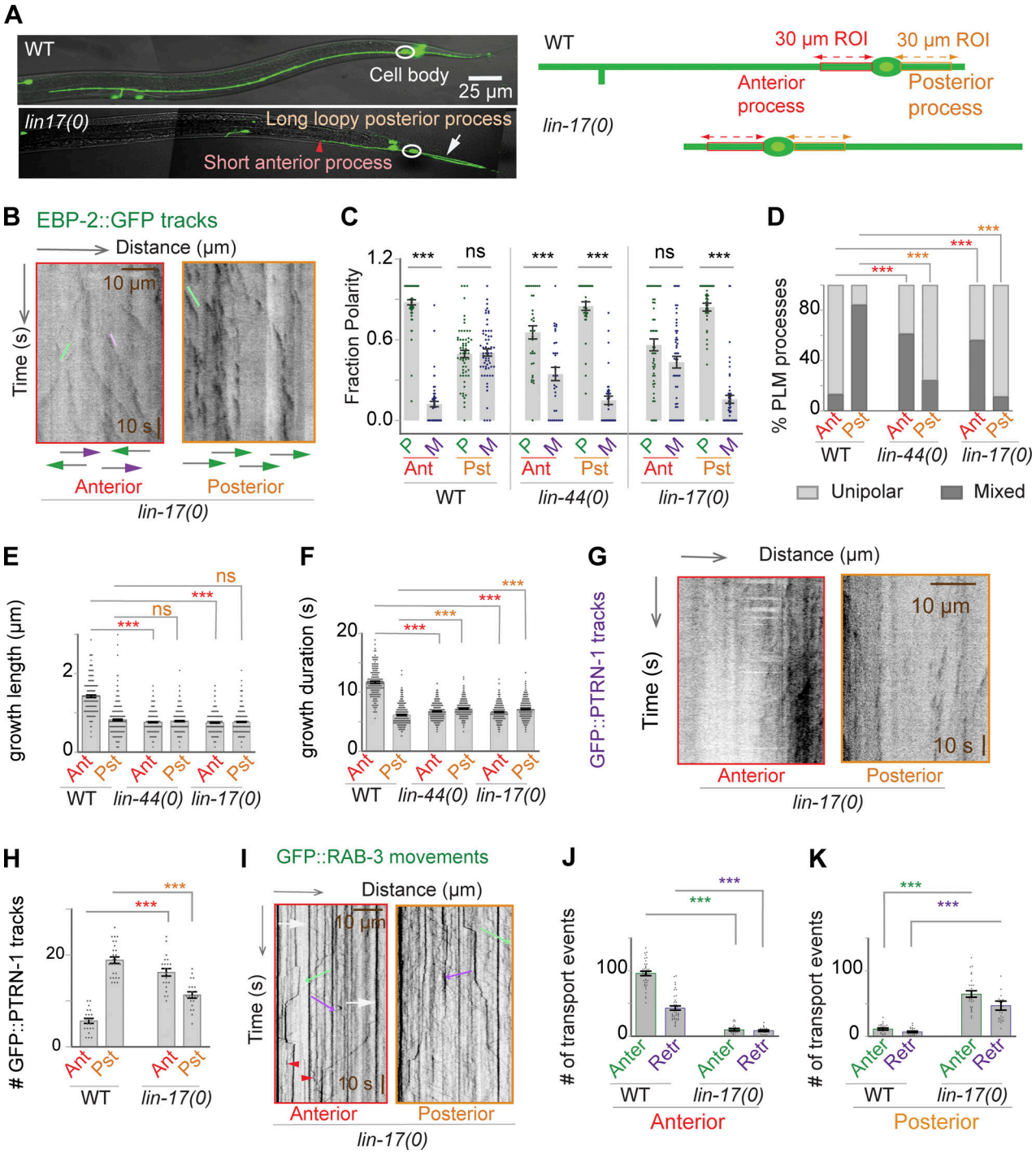

Figure 4. **Microtubule polarity in the PLM neuron is reversed in *wnt* mutants. (A)** Confocal image and illustration of neuronal polarity phenotype in *lin-17(0)*. The red arrowhead and the white arrow are indicating the short anterior process and long posterior process, respectively, in *lin-17(0)* background. **(B)** Kymographs of EBP-2::GFP movie (Video 1) showing the microtubule growth events in *lin-17(0)*. The green and magenta traces represent microtubules of plus-end-out and minus-end-out polarity, respectively. **(C and D)** The histogram shows the fraction of plus-end-out (P) and minus-end-out (M) microtubules (C) and the percentage of PLM processes with microtubules oriented in either a unipolar or mixed manner (D). N = 5–8 independent replicates; *n* (number of neurons) = 33–63. Ant, anterior; Pst, posterior. **(E and F)** Growth length and duration of microtubules measured from the EBP-2::GFP kymograph (B). N = 3 independent replicates; *n* (number of EBP-2 tracks) = 170–455. **(G and H)** Kymographs (G) and the quantification of the dynamics (H) of GFP::PTRN-1 (*juEx6455*) reporter in *lin17(0)* mutant. N = 3–5 independent replicates; *n* (number of neurons) = 20–27. **(I)** Kymographs obtained from the time-lapse movie of GFP::RAB-3 (*jsIs821*) reporter (Video 2) in *lin-17(0)* showing the events of anterograde (green arrow trace) and retrograde (magenta arrow trace) movement. White arrows show the static RAB-3 particles. The red arrowheads represent RAB-3 particles frequently switching direction. **(J and K)** The number of transport events of GFP::RAB-3 vesicles in anterograde (Anter) and retrograde (Retr) directions. N = 3–7 independent replicates; *n* (number of neurons) = 18–42. For C, E, F, H, J, and K, ***, P < 0.001; ANOVA with Tukey's multiple comparison test. For D, ***, P < 0.001; Fisher's exact test. Error bars represent SEM.

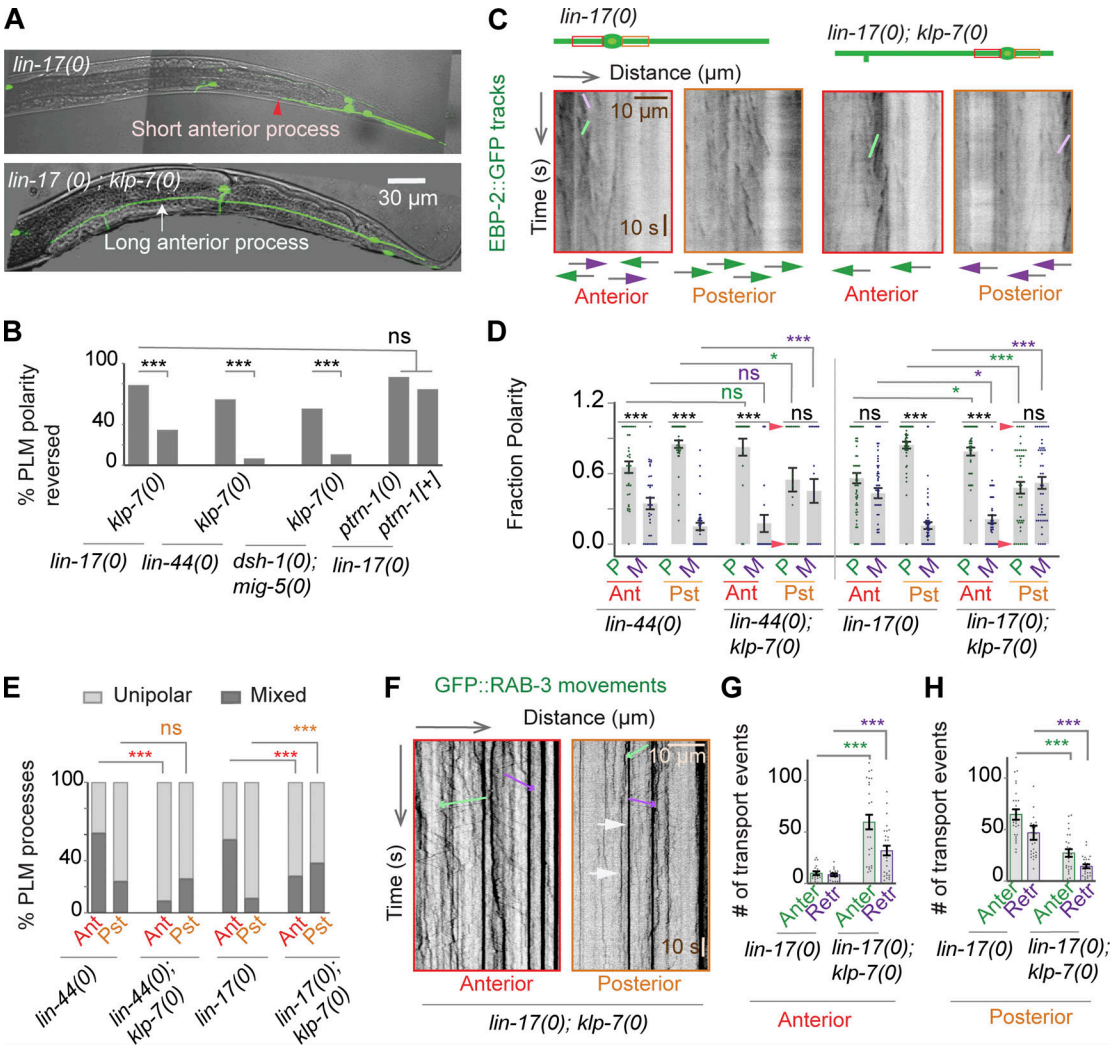

Figure 5. **Loss of *klp-7* rectifies the microtubule polarity switch phenotype in the *lin-17* mutant. (A)** Confocal images and schematics of neuronal polarity phenotype in *lin-17(0) and lin-17(0);klp-7(0)*. **(B)** The percentage of PLM neurons with polarity reversal phenotype due to altered *klp-7* or *ptrn-1* levels in *Wnt* mutants (*lin-17*, *lin-44*, *dsh-1mig-5*). N = 4–5 independent replicates; *n* (number of neurons) = 20–208. **(C)** Kymographs from EBP-2::GFP movies (Video 1) showing the microtubule growth events in *lin-17(0)* and *lin-17(0);klp-7(0)*. The green and magenta traces represent microtubules of plus-end-out and minus-end-out polarity, respectively. **(D and E)** The histogram shows the fraction of plus-end-out (P) and minus-end-out (M) microtubules (D) obtained from C and the percentage of PLM processes with microtubules oriented in either a unipolar or mixed manner (E). N = 7–8 independent replicates, *n* (number of neurons) = 19–52. Ant, anterior; Pst, posterior. **(F)** Kymographs of GFP::RAB-3 reporter (*jsIs821*) in *lin-17(0);klp-7(0)* background showing the events of anterograde (green arrow trace) and retrograde (magenta arrow trace) movement. The white arrows show the stationary particles. **(G and H)** The number of movement events of GFP::RAB-3 vesicles as obtained from F. Anter, anterograde; Retr, retrograde. N = 3–4 independent replicates; *n* (number of neurons) = 18–26. For B and E, ***, P < 0.001; Fisher's exact test. For D, G, and H, *, P < 0.05; ***, P < 0.001; ANOVA with Tukey's multiple comparison test. Error bars represent SEM.

anterior process due to loss of *klp-7* in both *lin-17(0)* and *lin-44(0)* backgrounds (Fig. 5, C–E). For example, the majority of the EBP-2::GFP comets showed plus-end-out movement in the anterior process of *lin-17(0);klp-7(0)* (Video 1; and Fig. 5, C and D). A similar trend was also noticed in the *lin-44(0);klp-7(0)* double mutant (Fig. 5 D). However, in the posterior process, the microtubule orientation showed unipolar organization with a bimodal distribution (red arrows showing the dispersion in Fig. 5 D) more akin to *klp-7(0)* (Fig. S2, C and D). These observations suggest the epistatic nature of *klp-7* to Wnt signaling in the posterior process. On the other hand, in the anterior process, there might be a negative regulation of KLP-7 by Wnt signaling to generate plus-end-out microtubules.

Live imaging of the GFP::RAB-3 reporter in the *lin-17(0);klp-7(0)* background (Video 2) revealed an increased number of anterograde and retrograde transport events in the anterior process as compared with that in *lin-17(0)* (Fig. 5, F and G). On the contrary, in the posterior process, transport events were significantly lower (Fig. 5, F and H). This shows that loss of *klp-7* not only suppresses the polarity defect in *lin-17(0)* but also is able to restore the normal axonal transport process driving the synaptic machinery to its correct destination.

Wnt/planar cell polarity (PCP) components involving Dishevelled-associated activator of morphogenesis 1 (daam-1)/*rho-1*/Rho-associated protein kinase (*rock*) act upstream of *klp-7* to restrain the length of the posterior process of PLM

The Wnt receptor LIN-17, which is localized in a gradient with its peak concentration at the posterior process of the PLM (Hilliard and Bargmann, 2006), might influence the localization of KLP-7. We found that the relative intensity of GFP::KLP-7 with respect to a soluble marker mScarlet in the anterior and posterior processes did not differ in any of the developmental stages (Fig. S3, A and B), and this pattern remained unchanged in *lin-17(0)* (Fig. S3, A and B), indicating that localization of KLP-7 is independent of Wnt signaling.

Alternatively, Wnt signaling could be regulating the activity of KLP-7 in a spatiotemporal manner in the PLM. The activity of Kinesin-13 is highly regulated by phosphorylation in both mitotic cells (Ems-McClung et al., 2013; Ritter et al., 2015) and neurons (Ogawa and Hirokawa, 2015). There are two kinds of conserved phosphorylation sites in the motor domain (Fig. S3 C). A-type phosphorylation increases the microtubule depolymerase activity of mouse Kinesin-13/kinesin family member 2A (KIF2A), and B-type phosphorylation inactivates the depolymerase (Ogawa and Hirokawa, 2015). A-type phosphorylation is catalyzed by Rho kinase at the T549 residue (Fig. 6 A), which is a downstream component of Wnt PCP signaling involving Dishevelled, DAAM-1, and Rho-1 (Schlessinger et al., 2009). Consistently, the anti–LET-502/ROCK antibody (Piekny and Mains, 2002) showed localization in the PLM neuron (arrow, Fig. S3 D). The GFP::LET-502 versus mCherry level was higher in the posterior process (Fig. 6, B and C). Moreover, the reporter NMY-2::GFP, which is a downstream effector of LET-502 (Michaux et al., 2018; Wernike et al., 2016; Nance et al., 2003), showed a distinct enrichment in the posterior process (arrowheads, Fig. 6, D and E; and Fig. S3 E). This pattern was reversed in *lin-17(0)* (Fig. 6, C and E).

The polarization of the PLM neuron is driven in part by restraining the growth of the posterior process by *daam-1* (Zheng et al., 2015). Neuron-specific RNAi of either *daam-1* or *rho-1* increased the length of the posterior process significantly (Fig. 6, F and G), leaving the length of the anterior process unchanged (Fig. S3 F). Similarly, PLM-specific knockdown of *let-502* using a hairpin loop construct of *let-502* increased the length of the posterior process (Fig. 6 H). The extension of the posterior process due to RNAi of *let-502*, *daam-1*, or *rho-1* is similar to what has been observed in the *klp-7(0)* or *klp-7* RNAi background (Fig. 6, G and H). Further, RNAi of these molecules could not enhance the phenotype in *klp-7(0)* (Fig. 6, G and H), indicating a linear relationship between *daam-1*, *rho-1*, *let-502*, and *klp-7* in regulating the length of the posterior process. Conversely, an activated version of RHO-1 (RHO-1^{G14V}; Alan and Lundquist, 2012) shortened the length of the posterior process in the WT background, but not in the *klp-7(0)* background (Fig. 6, F and I), whereas the anterior process remained unaffected (Fig. S3 G), indicating that *klp-7* is downstream to *rho-1*.

This relationship might involve enhancement of KLP-7 activity through phosphorylation at the threonine-549 residue by LET-502 (Fig. 6 A and Fig. S3 C). To test this possibility, we expressed a constitutively phosphorylated version (A type) of KLP-7 by substituting the threonine-549 with glutamic acid. Expression of KLP-7^{T549E} but not KLP-7^{T549A} significantly shortened the posterior process in the WT and *lin-17(0)* backgrounds (Fig. S3, H and I; and Fig. 6, J and K). However, the length of the anterior process remained unchanged in the *lin-17(0)* (Fig. 6 L) or WT background (Fig. S3, H and J). These results indicated that the regulation of KLP-7 activity by ROCK is restricted to the posterior process of the PLM. However, we noticed that in either the *lin-17(0)*;KLP-7^{T549E}[+] or the *lin-17(0)*;RHO-1^{G14V}[+] background, when the posterior process was very short, the anterior process grew longer (Fig. 6 J). This hinted at the reciprocal regulation between the neurites for differential growth (Shelly et al., 2010; Zheng et al., 2016). Taken together, our data suggested that the PCP components *daam1/rho-1/rock* act upstream of *klp-7* to restrain the growth of the posterior process (Fig. 6 M). Significant suppression of the neuronal polarity reversal phenotype in *lin-17(0)* by *klp-7(0)* indicates that negative regulation of KLP-7 by Wnt could stimulate the growth of the anterior process. Expression of KLP-7^{T549E} completely extended the anterior process and shortened the posterior process in *lin-17(0);klp-7(0)* (Fig. 6, K and L). 89% of PLM neurons attain normal polarized anatomy in this background (Fig. S3 K). This supports the theme that KLP-7 could be inhibited in the anterior process and simultaneously activated in the posterior process for proper polarization of the PLM.

unc-73/ced-10/p21-activated kinase 1 (*pak-1*) pathway negatively regulates *klp-7* in the anterior process

The phosphorylation of KIF2A by PAK-1 leads to the inactivation of its depolymerase activity (Fig. 7 A; Ogawa and Hirokawa, 2015). Using a translational reporter of *pak-1* (Zhang et al., 2011), we found that PAK-1::GFP is highly enriched in the anterior process (arrows, Fig. S4 A; and Fig. 7, B and C). In the absence of LIN-17, the PAK::GFP is enriched in the posterior process (Fig. 7, B and C). A similar observation was made using the anti–phospho-PAK (Thr423) antibody (Fig. S4, C–E). To find out the spatial distribution of the interaction between KLP-7 and PAK-1::GFP, we performed a proximity ligation assay (PLA; Chen et al., 2013; Day et al., 2020) between anti–KLP-7 and anti-GFP antibodies. We found that the PLA signal is specifically enriched in the anterior process (arrowheads, Fig. 7, D and E). This indicated that PAK-1 interacts with KLP-7 specifically in the anterior process of the PLM. PAK-1 is known to be activated by the Rac GTPase CED-10 (Newsome et al., 2000; Chen et al., 2011). CED-10 and the upstream GTP exchange factor UNC-73 are important for axonal growth of various neurons, including the PLM (Steven et al., 1998; Norris et al., 2014; Zheng et al., 2016). The loss of *klp-7* suppressed the short anterior axon phenotype seen in either *unc-73(0)* or *ced-10(0)* (Fig. 7, F–H). We made a constitutively phosphorylated version (B type) of KLP-7 at the substrate sites for PAK-1 (Fig. 7 A) by substitution of the serine residues at the 546th and 555th positions with glutamic acid. Expression of KLP-7$^{S546E\ S555E}$ in *unc-73(0)* extended the length of the anterior process significantly (Fig. 7 G). This suggested that

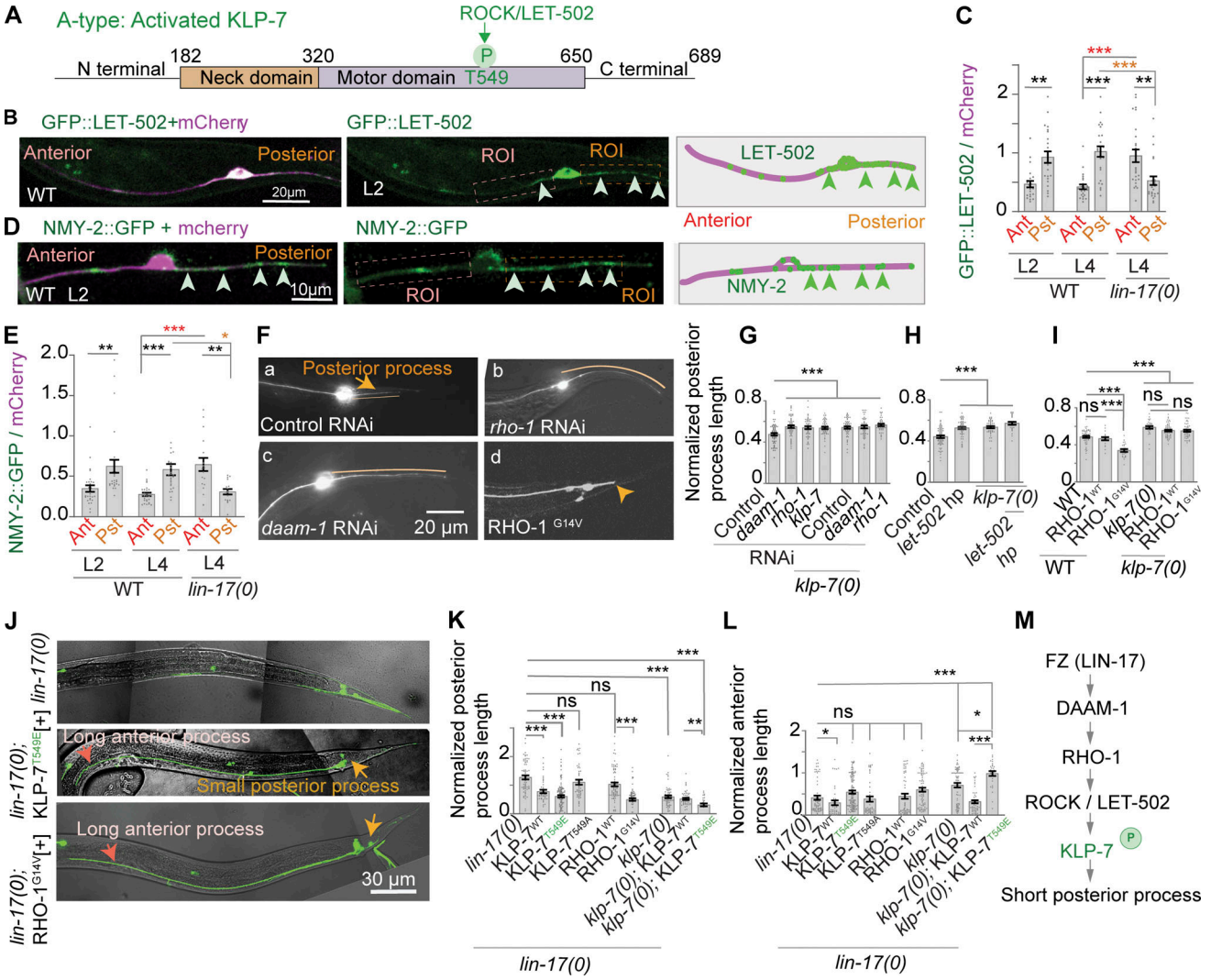

Figure 6. **Wnt PCP components act upstream of *klp-7* to restrain the growth of the posterior process. (A)** Phosphorylation site of ROCK on KLP-7. **(B)** Confocal images of the PLM expressing *Pmec-4*-GFP::LET-502 (*shrEx438*) and *Pmec-4*-mCherry (*tbIs222*). Arrowheads are indicating the enrichment of GFP::LET-502. **(C)** Relative intensity of GFP::LET-502 with respect to mCherry measured from the ROIs shown in B. Ant, anterior; Pst, posterior. **(D)** The processed images of worms expressing *Pnmy-2*-NMY-2::GFP (*zuIs45*) and *Pmec-4*-mCherry (*tbIs222*) for seeing PLM-specific localization of NMY-2. Arrowheads are indicating the enrichment of NMY-2::GFP. **(E)** Normalized fluorescence intensity of NMY-2::GFP with respect to mCherry from the ROIs shown in D. **(Fa–c)** Images of the PLM neuron in RNAi-sensitive strain *Pmec-18-sid-1(uIs71);lin15b(n744)* grown on HT115 bacteria expressing control (L4440), *daam-1*, and *rho-1* dsRNA. **(Fd)** Image of a PLM expressing an activated version of RHO-1. Arrowhead is pointing towards the short posterior process. **(G–I)** The change in normalized length of the PLM posterior process due to RNAi of PCP genes (G), P*mec-4*–driven expression of *let-502* hairpin loop RNA (H), and activated version of RHO-1 (I). For C, E, and G–I, N = 3–4 independent replicates; *n* (number of neurons) = 19–62. **(J)** Images of a PLM neuron in *lin-17(0)* expressing either the constitutively phosphorylated version of KLP-7, *Punc-86*-KLP-7^{T549E} (*shrEx203*), or an activated version of RHO-1, RHO-1^{G14V} (*shrEx284*). **(K and L)** Normalized posterior (K) and anterior (L) lengths of a PLM in a *lin-17(0)* background expressing *Punc-86*-KLP-7^{T549E} (*shrEx203*) or RHO-1^{G14V} (*shrEx284*). N = 3 independent replicates; *n* (number of neurons) = 28–115. **(M)** Pathway showing how PCP genes regulate KLP-7. *, P < 0.05; **, P < 0.01; ***, P < 0.001; ANOVA with Tukey's multiple comparison test. Error bars represent SEM.

unc-73/ced-10/pak-1 negatively regulates *klp-7* for the extension of the anterior process.

Rac GTPases often are activated by Wnt signaling (Habas et al., 2003). An active version of CED-10 caused an ectopic extension in the ALM and PLM neurons in the WT background (orange arrows, Fig. S4, F–J), which is similar to the *klp-7* mutant. It also extended the length of the anterior process in *lin-17(0)* significantly (Fig. 7, I and J). This indicated that in response to Wnt, CED-10 might inactivate KLP-7 through PAK-1 (Fig. 7, A and L). Expression of the inactive version (B-type) KLP-7$^{S546E\ S555E}$ in *lin-17(0)* led to a moderate extension of the anterior process (Fig. 7, I–K). However, simultaneous expression of the inactivated (B-type) version with the activated version (A-type) KLP-7^{T549E} increased the length of the anterior process significantly as compared with the length in *lin-17* mutant (Fig. 7 J and Fig. S4 K). This again supported that the inactivation of KLP-7 in the anterior process and simultaneous activation of the same in the posterior process help in the polarization of PLM neuron.

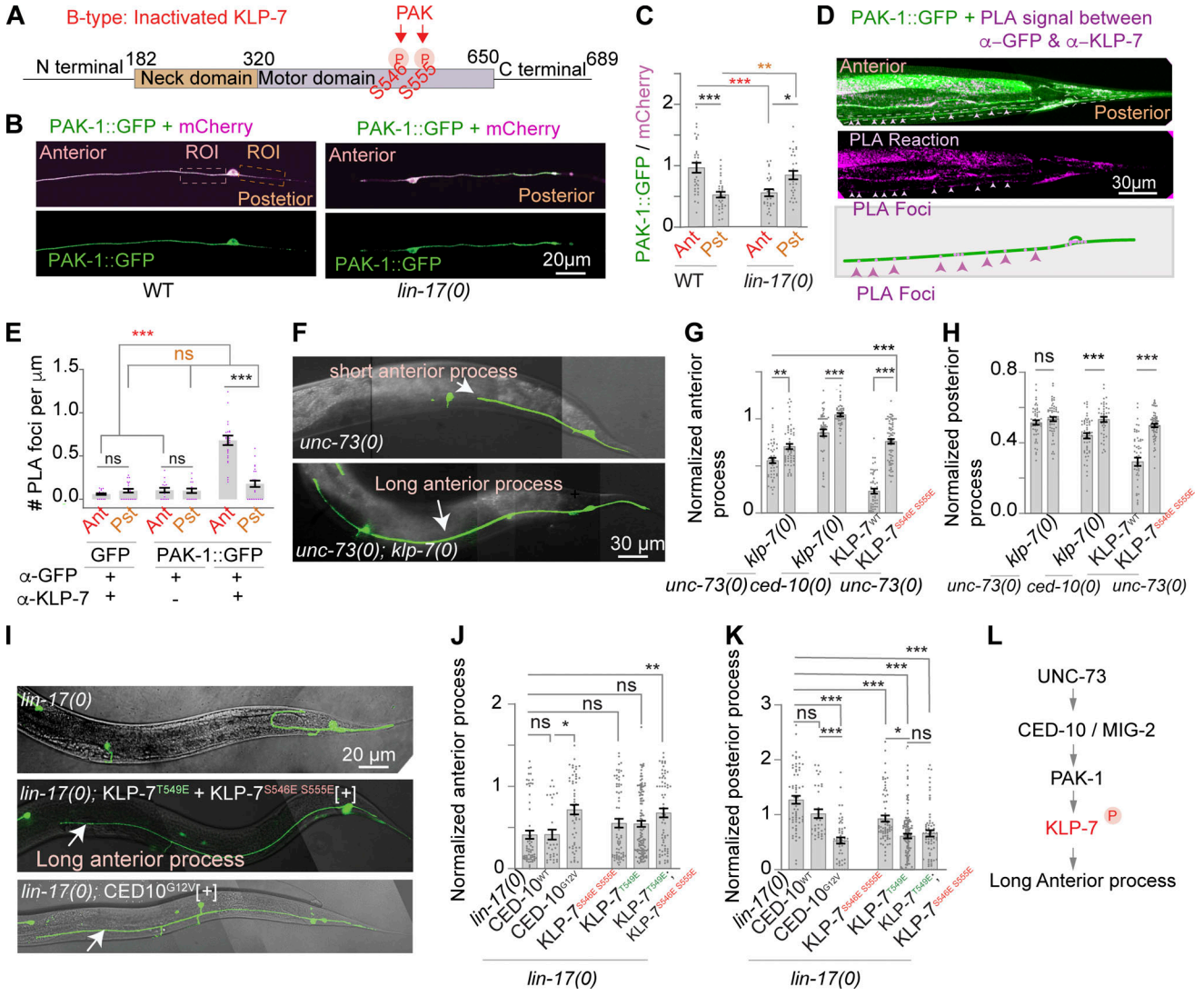

Figure 7. ***unc-73* pathway negatively regulates *klp-7* to promote the growth of the anterior process. (A)** Phosphorylation sites of PAK on KLP-7. **(B)** The processed images of a worm expressing *Ppak-1*-PAK-1::GFP (*shrEx439*) and *Pmec-4*-mCherry (*tbIs222*) for seeing PLM-specific localization of PAK-1. **(C)** The relative intensity of PAK-1::GFP with respect to mCherry from the ROIs shown in B. Ant, anterior; Pst, posterior. **(D)** Image of the PLA between α-GFP and α-KLP-7 antibodies in a worm expressing PAK-1::GFP. Arrowheads indicate the PLA foci in the PLM anterior process. **(E)** The count of PLA foci per micrometer of PLM processes shown in D. **(F)** Confocal images of a PLM neuron in *unc-73(0)* and *unc-73(0);klp-7(0)*. **(G and H)** Normalized anterior (G) and posterior (H) lengths of the PLM in the single mutant of *unc-73* pathway or combination with either *klp-7(0)* or a transgene *shrEx266* (*Punc-86*-KLP-7$^{S546E\ S555E}$) expressing a B-type inactive version of KLP-7. For C, E, G, and H, N = 3–4 independent replicates; *n* (number of neurons) = 42–68. **(I)** Confocal images of a PLM neuron in *lin-17(0)* coexpressing the A-type hyperactive *Punc-86*-KLP-7^{T549E} and B-type inactive *Punc-86*-KLP-7$^{S546E\ S555E}$ versions of KLP-7 using *shrEx197* or expressing the activated version of CED-10, CED-10^{G12V} (*shrEx294*). **(J and K)** Normalized anterior (J) and posterior (K) lengths of the PLM in *lin-17(0)* background expressing various mutant forms of KLP-7 and CED-10. N = 3–4 independent replicates; *n* (number of neurons) = 32–115. **(L)** Pathway showing how UNC-73/CED-10 regulates KLP-7. *, P < 0.05; **, P < 0.01; ***, P < 0.001; ANOVA with Tukey's multiple comparison test. Error bars represent SEM.

rock/let-502 induces mixed polarity of microtubules in the posterior process, and *unc-73/ced-10* promotes unipolar organization of microtubules in the anterior process

We speculated that the *let-502* pathway might be required to induce mixed polarity of microtubules in the posterior process. Neuron-specific knockdown of *daam-1*, *rho-1*, or *let-502* increased the fraction of the posterior processes with a unipolar microtubule (Fig. 8, B and C). Half of the processes had all plus-end-out microtubule organization (class 1), and the rest had minus-end-out microtubule organization (class 2; Fig. 8 B; Fig. S5 B). Consistently, the frequency distribution of the posterior processes with plus-end-out microtubules showed two-mode values of 0.8 and 0.2 (Fig. S5 B). Conversely, a constitutively active version of RHO-1 or a phosphorylated version of KLP-7 (A type) reduced the growth length of microtubules and increased the number of EBP tracks (Table S2) specifically in the posterior process (Fig. S5, C and D). When either of these constructs was expressed in *lin-17(0)*, the fraction of microtubules with plus-end-out polarity was decreased in the posterior process (Fig. S5 E). As a result, the fraction of posterior processes with mixed microtubule polarity increased significantly (Fig. 8 D). This strengthened the conclusion that the

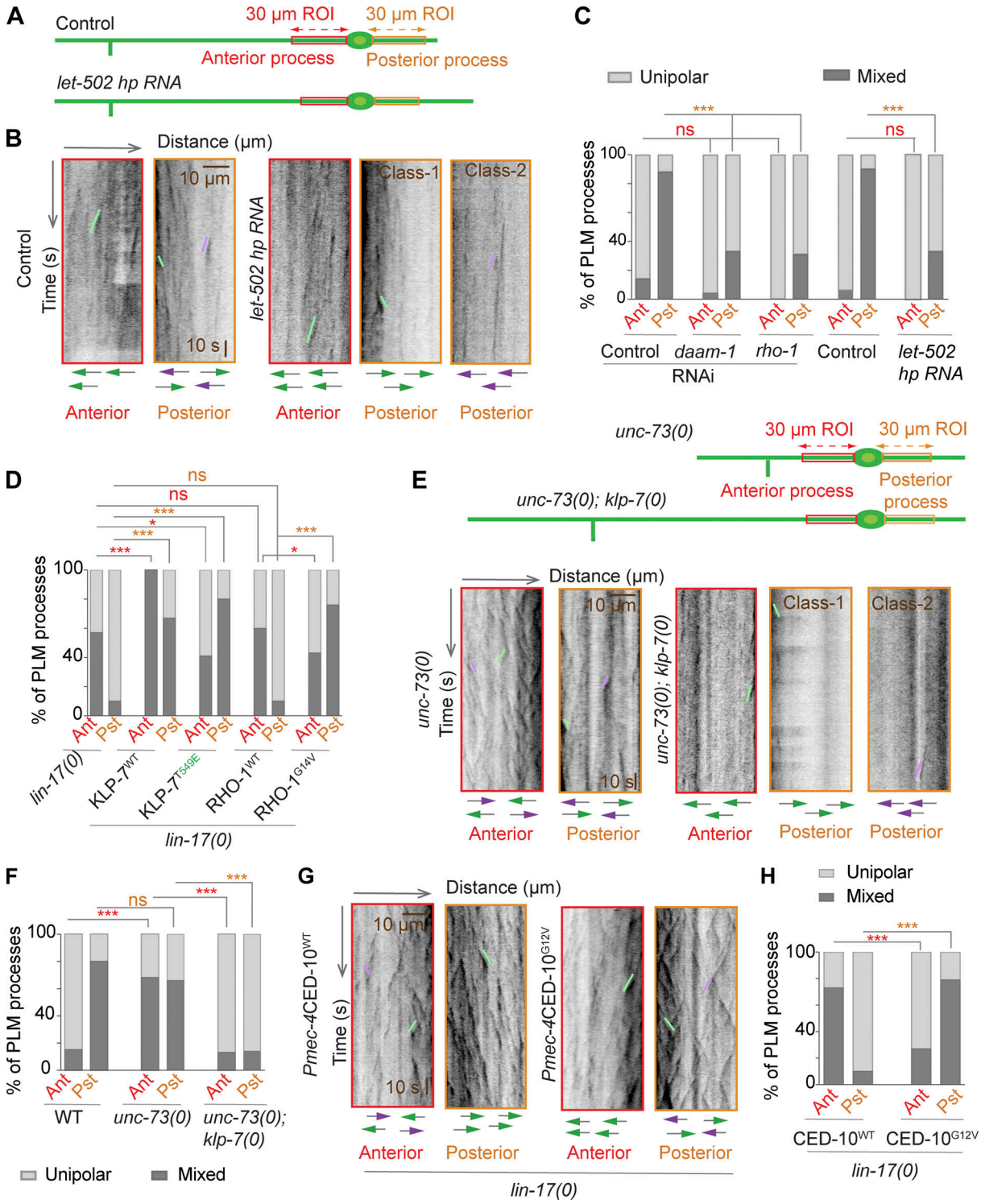

Figure 8. **Downstream components of Wnt signaling regulate microtubule polarity. (A and B)** Illustration of the ROIs and the kymographs showing the EBP-2 tracks in control and *let-502* hairpin loop (hp) RNAi-expressing neurons. **(C and D)** The quantification of the effect on microtubule arrangement in the PLM processes due to *Pmec-4*–driven expression of *let-502* (hp) RNA, due to RNAi of genes involving PCP (C), due to expression of the A-type active version of KLP-7 P*mec-4*-KLP-7^{T549E} (*shrEX303*), and due to the activated version of RHO-1 *Pmec-4*-RHO-1^{G14V} (*shrEx332*) in a *lin-17(0)* background (D). For C and D, N = 3–4 independent replicates; *n* (number of neurons) = 20–39. Ant, anterior; Pst, posterior. **(E)** Kymographs of EBP-2::GFP dynamics in *unc-73(0)* and *unc-73(0); klp-7(0)* backgrounds. **(F)** The percentage of PLM processes with microtubules oriented in either a unipolar or mixed manner in *unc-73(0)* and *unc-73(0);klp-7(0)* backgrounds. N = 3–5 independent replicates; *n* (number of neurons) = 19–46. **(G)** Kymographs of EBP-2::GFP in *lin-17(0)* background expressing the WT (*shrEx344*) or activated version of CED-10 (*shrEx*346) in touch neurons. **(H)** Quantification of the percentage of PLMs with microtubules oriented in either a unipolar or mixed manner. N = 3 independent replicates; n (number of neurons) = 28–33. For B, E, and G, the green and magenta traces represent microtubules of plus-end-out and minus-end-out polarity, respectively. For C, D, F, and H, *, P < 0.05; ***, P < 0.001; Fisher's exact test.

rho1-rock pathway positively regulates *klp-7* to induce mixed polarity of microtubules in the posterior process.

Loss of *unc-73* induced mixed polarity of microtubules in the anterior process (Fig. 8, E and F; and Fig. S5 F). Growth length and duration of the microtubules were significantly decreased in the anterior process in *unc-73(0)* (Fig. S5, G and H), and the number of EBP tracks was increased (Table S2). This indicated that loss of *unc-73* increases microtubule dynamics in the anterior process probably due to the abnormal activation of KLP-7. Consistent with this hypothesis, the fraction of the anterior process with mixed microtubule polarity was suppressed by the loss of *klp-7* in *unc-73(0)* (Fig. 8, E and F). Since *unc-73/ced-10*–mediated regulation of microtubule polarity might occur as a downstream effect of the LIN-17 pathway, we tested whether the parameters of microtubule dynamics in *lin-17(0)* can be changed by activating CED-10. The expression of an activated version of CED-10 (CED-10^{G12V}) in *lin-17(0)* increased the fraction of microtubules with plus-end-out polarity in the anterior process (Fig. 8 G; and Fig. S5, I–K). Therefore, it suppressed the value of the percentage of anterior processes with mixed polarity (Fig. 8 H). Overall, we concluded that the *unc-73* pathway negatively regulates *klp-7* to promote plus-end-out organization of microtubules in the anterior process.

UNC-73 and ROCK differentially regulate KLP-7 dynamics in the anterior and posterior processes, respectively

To assay the differential regulation of KLP-7 in the anterior versus posterior process, we performed time-lapse imaging of a functional construct of GFP::KLP-7, which rescued the developmental phenotype in *klp-7(0)* to 75% of the WT level. Live imaging of GFP::KLP-7 revealed that KLP-7 shows bidirectional short-range movement in both the processes of the PLM (Video 3 and Fig. 9 B). This is consistent with the biophysical analysis of mitotic centromere-associated kinesin (MCAK)/KLP-7 bound to microtubules that MCAK readily slides along the microtubules in either direction to capture the ends (Oguchi et al., 2011; Helenius et al., 2006). Therefore, these tracks in the kymograph (Fig. 9 B) represent the active KLP-7 population on microtubules. These movements were undetectable upon colchicine treatment (Fig. 9 C), indicating that these are microtubule-related events. The number of GFP::KLP-7 tracks in the posterior process was significantly higher than that in the anterior process (Fig. 9, B and C). This indicated that in the posterior process, there is a greater number of microtubule ends being captured by KLP-7. The length of the tracks was visually and quantitatively shorter in the posterior process (Fig. 9, B and D). Loss of *unc-73* specifically increased the number of tracks in the anterior process (Fig. 9, E and G). These tracks were relatively shorter than those in the WT background (Fig. 9, E and H). Conversely, a constitutively inactive version (B type), KLP-$7^{S546E\ S555E}$, which is phosphorylated at the substrate sites of PAK-1, shows an opposite behavior. The number of tracks was less, and the tracks were longer (Fig. 9, F–H).

The loss of Rho kinase-1/*let-502* using a hairpin loop RNAi led to a specific decrease in the track number in the posterior process, leaving the dynamics of KLP-7 in the anterior process unchanged (Fig. 9, I–K). These observations gave direct evidence that KLP-7 is differentially regulated by UNC-73 and ROCK in the anterior and posterior processes, respectively (Fig. 9 L).

Discussion

Overall, our findings show that the microtubule-depolymerizing motor protein KLP-7 maintains the dynamic state of the microtubules in touch neurons. The microtubule-depolymerizing activity of KLP-7 gets boosted in the posterior process of the PLM by the Wnt signaling, which generates more growing microtubules with mixed polarity. The growing minus ends are captured and maintained by CAMSAP2/PTRN-1,whereas in the anterior process, *unc-73/ced-10* negatively regulates *klp-7*, generating plus-end-out microtubules and promoting vesicular transport for the growth of the anterior process. This study provides a mechanistic link between the Wnt signaling and Kinesin-13 for the proper organization of microtubule polarity (Fig. 10).

Kinesin-13 is an important determinant of microtubule polarity in neurons

The organization of the microtubule cytoskeleton within a neuron is important for the polarized distribution of presynaptic and post-synaptic organelles (Maeder et al., 2014). EBPs stabilize microtubules in axons (Leterrier et al., 2011; Yau et al., 2014; Maniar et al., 2012; van Beuningen et al., 2015). However, the role of microtubule catastrophe factors is less explored in neuronal polarization processes. Kinesin-13 is a critical determinant of dynamic instability in microtubules (Desai et al., 1999; Trofimova et al., 2018; Ogawa et al., 2017). In the mouse, knockdown of Kinesin-13 homologue KIF2A causes abnormal brain development (Homma et al., 2003). Our study revealed that the Kinesin-13 homologue in *C. elegans* is necessary to maintain the microtubules in the posterior process of the PLM neuron in a mixed polarity state. In the dendrites of the PVD neuron, we found an accumulation of axonal cargo in the *klp-7* mutant, indicating that the dendrite takes on an axon-like identity. This is consistent with the finding that conditional knockout of KIF2A in the mouse dentate gyrus results in the conversion of dendrites to the axon (Homma et al., 2018). In the presence of active KLP-7, the microtubules can be short enough that they can overcome cross-linking activity by proteins such as TRIM46 (van Beuningen et al., 2015) and move around to contribute to mixed polarity. Several reports have indicated the role of Kinesin-13 in limiting the nucleation and length of cellular microtubules (Vasudevan et al., 2015; Domnitz et al., 2012; Srayko et al., 2005). In dendrites, the dynamic and tyrosinated population of microtubules adopts mixed polarity (Tas et al., 2017). Coincidentally, the tyrosinated microtubules are preferentially recognized by Kinesin-13 (Peris et al., 2009). In our view, Kinesin-13–mediated microtubule depolymerization generates the "microtubule seeds" for mixed polarity organization in dendrites. Then the plus and minus ends are maintained by plus tip proteins and CAMSAP2, respectively. Many reports have recently indicated the role of CAMSAP2 in maintenance of the minus ends in dendrites (Cao et al., 2020; Feng et al., 2019; Yau et al., 2014; Wang et al., 2019).

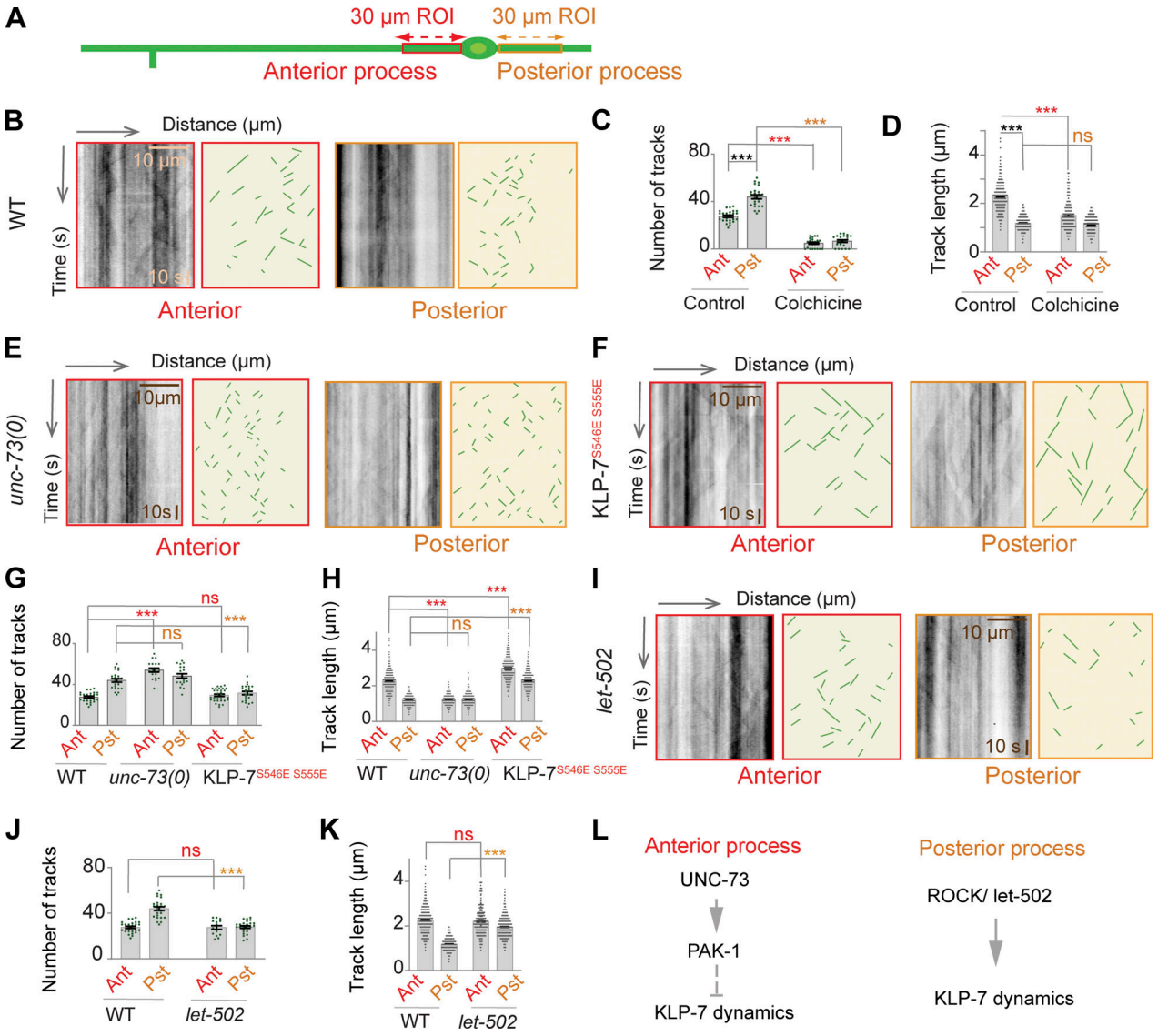

Figure 9. **Differential regulation of KLP-7 dynamics in the anterior and posterior processes of the PLM. (A–D)** The ROI schematics (A), kymographs (B), and analysis (C and D) of GFP::KLP-7 dynamics (Video 3) in control and colchicine-treated worms. The green traces of the GFP::KLP-7 movements are illustrated next to the kymographs. N = 4–8 independent replicates. For C, *n* (number of neurons) = 20–27; for D, *n* (number of GFP::KLP-7 tracks) = 132–618. Ant, anterior; Pst, posterior. **(E–K)** Kymographs and analysis of GFP::KLP-7 dynamics in *unc-73(0*; E, G, and H), KLP-7$^{S546E\ S555E}$[+] (F, G, and H) and *let-502* RNAi (I, J, and K) backgrounds. N = 4–6 independent replicates. For G and J, *n* (number of neurons) = 15–27. For H and K, n (number of GFP::KLP-7 tracks) = 383–675. **(L)** Pathway showing the regulation of KLP-7 dynamics by PAK-1 and ROCK. For C, D, G, H, J, and K, ***, P < 0.001; ANOVA with Tukey's multiple comparison test. Error bars represent SEM.

Wnt signaling regulates microtubule polarity in neurons through Kinesin-13

Anterior–posterior guidance of commissural axons in the spinal cord is driven by the Wnt signaling (Lyuksyutova et al., 2003). In the case of commissural axons, Wnt acts as an attractive signal by binding to its receptor Frizzled present in the growth cone (Lyuksyutova et al., 2003). However, for the growth of the corticospinal tract, the protein Ryk acts as a repulsive receptor of Wnt (Liu et al., 2005). The downstream component of the Wnt pathway is Dishevelled, which activates either the canonical β-catenin pathway or the noncanonical PCP pathway (Schlessinger et al., 2009). In PLM neurons, LIN-44 (ligand)/LIN-17 (receptor) restrain the growth of the posterior process and promote the growth of the anterior process (Hilliard and Bargmann, 2006; Zheng et al., 2015). We found that the Wnt pathway keeps the microtubules in a dynamic state in the posterior process and that the anterior process is maintained in a stable form. This is consistent with the previous findings that Wnt signaling can both stabilize and destabilize the microtubule cytoskeleton during axonal growth (Ciani et al., 2004; Purro et al., 2008; Greer and Rubin, 2011; Stanganello et al., 2019).

We further showed that the PCP component of Wnt positively regulates *klp-7* to keep the microtubules in a mixed polarity state in the posterior process. The activity of Kinesin-13/KIF2A in neurons is enhanced by ROCK through phosphorylation (Ogawa and Hirokawa, 2015). This agrees with our observation

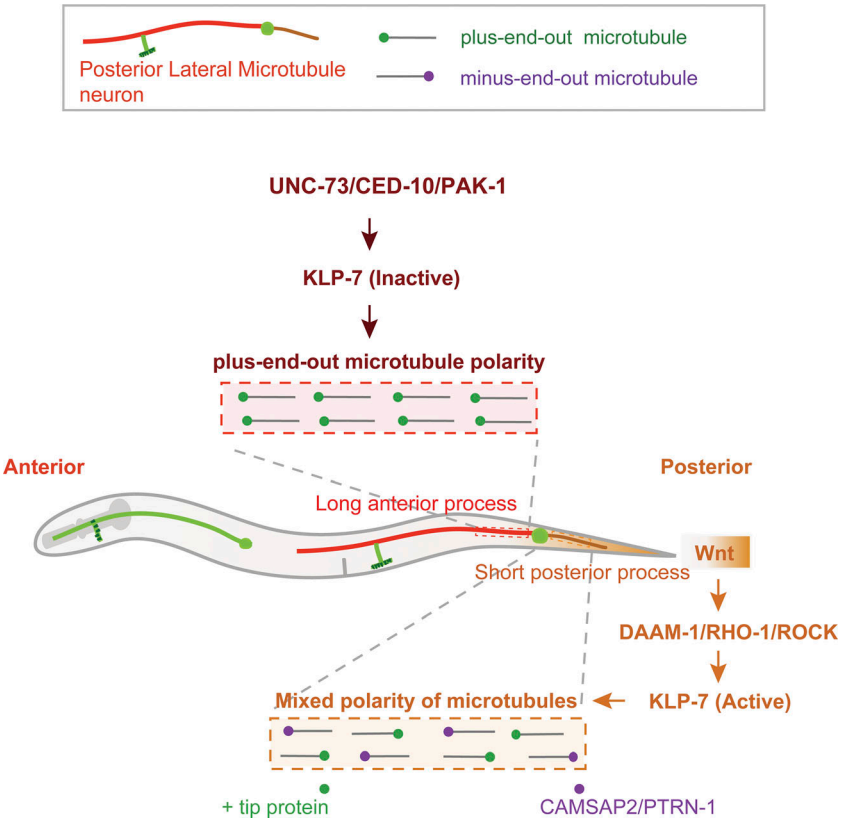

Figure 10. **Regulation of Kinesin-13 and microtubule polarity in the PLM neuron.** In the posterior process of the PLM neuron, the components of Wnt signaling induce mixed polarity of microtubules through the up-regulation of KLP-7 activity, whereas in the anterior process, KLP-7 is negatively regulated by the CED-10/PAK-1 cascade in order to polarize the microtubules in a plus-end-out manner.

that loss of ROCK reduces the KLP-7 dynamics and stabilizes the microtubules in the posterior process. This is also consistent with the previous finding that the Rho1 pathway downstream of Wnt3a restrains the growth of the dendrites by destabilizing the microtubules (Purro et al., 2008). We found that CED-10 (RAC) negatively regulates KLP-7 to stabilize the microtubules in the anterior process. This is consistent with the knowledge that Rac is an effector of Wnt signaling (Levy-Strumpf et al., 2015; Čajánek et al., 2013; Habas et al., 2003). The kinase that acts downstream of CED-10 activity is PAK-1 (Newsome et al., 2000; Chen et al., 2011). PAK-1 is shown to inhibit the microtubule depolymerization activity of KIF2A in the neurons (Ogawa and Hirokawa, 2015). We found that PAK-1 is enriched in the anterior process in a Wnt-dependent manner. This further supported that Wnt signaling might regulate KLP-7 in the anterior process through the CED-10/PAK-1 pathway. In *C. elegans*, *pak-1* is redundant with *max-2* and *pak-2* (Chen et al., 2011), making it difficult to test the role of these redundant kinases in PLM growth.

Materials and methods

C. elegans genetics

C. elegans strains were grown on nematode growth medium (NGM) plates seeded with OP50 *E. coli* bacteria at 20°C using standard methods (Brenner, 1974). All the loss-of-function alleles except the conditional mutants were denoted as *0*. For example, the *klp-7(tm2143)* mutant is presented as *klp-7(0)*. All the mutants and transgenic reporter strains used in this study are mentioned in Table S4. All newly generated transgenic strains carrying the extrachromosomal DNA used in this study are mentioned in Table S5. Transgenes were introduced into the mutant backgrounds by crossing. Homozygosity for all mutations was confirmed by either PCR or sequencing. We used the following published transgenes: *Pmec-7*-GFP (*muIs32*), *Pmec-4*-mCherry (*tbIs222*; Basu et al., 2017), *Pmec-4*-EBP-2::GFP (*juIs338*; Chuang et al., 2014), *Pmec-7*-GFP::RAB3 (*jsIs821*; Mondal et al., 2011), and *Pmec-7*-TagRFP::ELKS-1 (*jsIs1075*; Zheng et al., 2014).

Generation of a new allele of *klp-7* using CRISPR

We generated the *klp-7(shr3)* allele using the CRISPR/Cas9 protocol widely used by many laboratories (Friedland et al., 2013). We cloned the sgRNA 5′-AACCCATCACTCCAAGCACC-3′ specific to the third exon of *klp-7* into the pU6-sgRNA vector to generate pU6-*klp-7* sgRNA (pNBR2). We injected CRISPR/Cas9 *Peft-3*::cas-9::NLS (Friedland et al., 2013) and pU6-*klp-7* sgRNA and coinjection marker *Pttx-3*::RFP in the N2 background and identified a 28-bp deletion (from 2,830 bp to 2,858 bp) in exon 3 of the *klp-7* gene by genotyping the single-selfed filial 1 (F1) progenies. For genotyping the *shr3* allele, PCR was performed using forward primer 5′-AACCCATCACTCCAAGCACC-3′ and reverse primer 5′-GCTCCACCAATCGCCAACAT-3′ followed by a restriction fragment length polymorphism using the TaqI restriction enzyme.

Molecular cloning and mutagenesis

For touch neuron–specific expression of *klp-7*, Gateway (Thermo Fisher Scientific; K2500-20) entry clones of *klp-7* cDNA were

recombined with pCZGY553 (*Pmec-4* destination vector) and pCZGY61 (*Punc-86* destination vector) using LR clonase (Invitrogen; 11791-020). The entry clones pCZGY1718 and pCZY1723 (Ghosh-Roy et al., 2012) were used for the expression of *klp-7a* (747 aa) and *klp-7b* (689 aa) isoforms, respectively. To make *Pmec-4*-GFP::KLP-7B, the entry clone pCZGY1723 corresponding to *klp-7b* cDNA was recombined with pCZGY1867 (*Pmec-4* GFP destination vector). To make *Pmec-4*-GFP::LET-502 (pNBRGWY150), we first made a PCR8 entry clone pNBRGWY86 by amplifying *let-502* using primers 5′-GGCATGGAGCAGGATGAGCTGCGT GATC-3′ and 5′-CTATTGATAGATTGTGGAAGAGTTTGACGA TCC-3′ from the YK31144p06 clone (Yuji Kohara collection). Next, this entry clone was recombined with pCZGY1867 (*Pmec-4* GFP destination vector) to generate *Pmec-4*-GFP::LET-502.

We used the Q5 site-directed mutagenesis kit (E0554S; New England Biolabs) on the entry clone pCZGY1723 (PCR8::*klp-7b*) construct for generating hyperactive (class A, constitutively phosphorylated at the substrate site for ROCK) and hypoactive (class B, constitutively phosphorylated at the substrate site for PAK-1) forms of KLP-7B. For class A mutation KLP-7^{T549E}, we changed the threonine residue at the 549th aa of KLP-7B to glutamic acid. To make the phosphodead version KLP-7^{T549A} in the same position, threonine was replaced with alanine. We used 5′-GTCGAAGCTCGAGATGGTTCTCC-3′ and 5′-TGTCTGAACGGG ACATGT-3′ primers to generate pNBRGWY61 (PCR8::KLP-7b ^{T549E}), and to generate pNBRGWY75 (PCR8::KLP-7b ^{T549A}), we used 5′-GTCGAAGCTCGCTATGGTTCTCC-3′ and 5′-TGTCTGAAC GGGACATGT-3′ primers. To generate class B–type mutations, we changed the serine residues at the 546th and 555th positions to glutamic acid by overlapping PCR on pCZGY1723 (pCR8::KLP-7B) as a template. We used 5′-AATGCTTGTCGTCGGGATG-3′ and 5′-CACCGATGAACTCGTCTCGGAGAACCATCGTGAGCTTCTCCT GTCTGAAC-3′ to generate a PCR fragment with a mutation corresponding to KLP-7^{S546E}. Similarly, we used 5′-GTTCAGACAGGA GAAGCTCACGATGGTTCTCCGAGACGAGTTCATCGGTG-3′ and 5′-GTAGCATATCGTCGCGGGAATC-3′ to generate another fragment having a mutation corresponding to KLP-7^{S555E}. Then these two fragments were annealed by complementary homology ends. The resultant annealed PCR product was cloned in a pCR8 vector (Thermo Fisher Scientific; K2500-20) to get pNBRGWY66 (PCR8::KLP-7b$^{S546E\ S555E}$). Furthermore, we recombined the entry clones of *klp-7b* having the mutations described above with pCZGY61 (*Punc-86*-Gateway destination vector) and pCZGY553 (*Pmec-4* destination vector) to obtain neuronal expression clones. The plasmids were injected at the concentrations mentioned in Table S5 with the coinjection marker Pttx-3::RFP or Pttx-3::GFP at 50 ng/µl. The total concentration of injected DNA was maintained at 110–120 ng/µl by adding pBluescript SK plasmid to the injection mixture.

RNAi experiments

To knock down the genes controlling the PCP/Wnt signaling pathway, we performed RNAi, since the mutants deleting these genes are lethal. We used *lin-15b(n744);tbIs222 (Pmec-4::mcherry); uIs71[(pcFJ90)myo-2p::mcherry+mec-18p::sid-1]*, *klp-7(tm2143);lin-15b(n744);tbIs222; uIs71*, and *lin15b(n744);uIs71;juIs338* strains for RNAi. We used HT115 *E. coli* bacteria expressing dsRNA of *dhc-1* as a positive control because RNAi against *dhc-1* produces dead embryos (Gönczy et al., 1999). HT115 having the empty plasmid L4440 was used as a negative control. The bacterial strains carrying the dsRNA constructs used in this study are part of Ahringer's library (Kamath et al., 2001), which was purchased from Source BioScience (3318_Cel_RNAi_complete). The primary bacterial culture was grown at 37°C in lysogeny broth (LB) containing ampicillin (100 µg/µl), and tetracycline (12.5 µg/µl) for 8 h. The secondary culture was prepared by inoculating 1 ml of the primary culture to the 4 ml of LB containing 1 mM IPTG and kept for 1 h to reach an OD_{600} value of 0.4. The culture was pelleted and resuspended with 1 ml LB containing 1 mM IPTG and the aforementioned antibiotics. The resuspended 200-µl culture was spotted onto the NGM plates containing antibiotics and IPTG. The plates were dried for 7–10 h at 25°C. We transferred three L1s to these plates and imaged their progenies at the L4 stage. Bacteria expressing the dsRNA against *klp-7*, *daam-1*, and *rho-1* used are part of Ahringer's library (Kamath et al., 2001). Neuronal knockdown was verified by the observation that RNAi against *klp-7* showed ectopic process outgrowth from the cell bodies of touch neurons as noted in the genetic mutant of *klp-7*.

Touch neuron–specific knockdown of *let-502* using hairpin loop dsRNA

For effective knockdown of *let-502*, we selected exon 3 of the *let-502* gene according to the region targeted in Ahringer's library (Kamath et al., 2001) and made a hairpin loop construct pNBRGWY78 *Pmec4::let-502(5′-3′* exon-3*)-spacer-let-502(3′-5′* exon3*)*. We amplified the *let-502(5′-3′* exon-3*)* using 5′-CAAACGAGC TGACTCTGCATTC-3′ and 5′-CTTCTCTGAGAGTGGCAAATG TCC-3′. We selected intron 2 of the *klp-7* gene as a spacer. We amplified the spacer using 5′-GCCACTCTCAGAGAAGCGATCCCG ACGCGAC-3′ and 5′-GCCACTCTCAGAGAAGAGTCGATTTACGGG CTCGG-3′ primers and *let-502(3′-5′* exon3*)* using 5′-CCGAGCCCG TAAATCGACTCTTCTCTGAGAGTGGC-3′ and 5′-TTTTTTCGA GCTGACTCTGCATTCTTC-3′ primers. Then these two fragments were annealed by complementary homology ends. Next, we cloned the two fragments *let-502(5′-3′* exon-3*)* and *spacer-let-502(3′-5′* exon3*)* in pCZGY553 (*Pmec-4*-GWY) using infusion cloning (Takara Bio USA; 638916). The backbone pCZGY553 (*Pmec-4*-GWY) was amplified using 5′-GAATGCAGAGTCAGC TCGAAAAAACTTGTACAAAGTGGTGATGT-3′ and 5′-GCAGAG TCAGCTCGTTTGAAACTTGTGATGTACCGTCG-3′ primers. The resultant plasmid pNBRGWY78 *Pmec4::let-502(5′-3′* exon-3*)-spacer-let-502(3′-5′* exon3*)* was injected at 15 ng/µl along with Pttx-3::GFP as a coinjection marker in the *lin-15B(n744); tbIs222(mec-7p::mcherry);uIs71[(pcFJ90)myo-2p::mcherry+mec-18p::sid-1]* background.

Immobilization of worm for imaging

L4 stage worms expressing fluorescent markers were mounted in 10 mM levamisole (Sigma-Aldrich; L3008) on 5% agarose for confocal scanning or widefield imaging. A 0.1-µm polystyrene bead suspension (Polysciences; 00876-15) was used on 12.5% agarose pads made in M9 buffer for live imaging of either the EBP-2::GFP, GFP::PTRN-1, or GFP::KLP-7 reporter using the

protocol described earlier (Ghosh-Roy et al., 2012). The mounting conditions were varied for best immobilization and fluorophore visualization. For live imaging of the GFP::RAB-3 reporter, 10 mM levamisole was used according to a previously discussed method (Basu et al., 2017).

Widefield imaging of touch receptor neurons (TRNs) for quantifying developmental defects

Phenotyping of TRNs was done at the L4 stage, unless otherwise mentioned, using a Leica DM5000B microscope with a 40× objective (NA 0.75). During imaging, worms were immobilized using 0.05% sodium azide (Sigma-Aldrich; S2002) in a 5% agarose (Sigma-Aldrich; A4718) pad. The presence of a long polarized anterior process with ventral branch and the relatively short posterior process in the PLM neuron was scored using this approach. This allowed us to judge the polarity defects due to the loss in Wnt signaling and interaction between *klp-7(0)* and *lin-17(0)* (Fig. 5, A and B). Similarly, ectopic process outgrowth of ALM due to loss of *klp-7* was quantified using this approach (Fig. 1, A and B).

Drug treatment

Worms were grown on NGM plates containing different concentrations of colchicine (Sigma-Aldrich; C9754) and Taxol (Sigma-Aldrich; CAS33069-62-4) dissolved in ethanol and DMSO, respectively, as described previously (Kirszenblat et al., 2013). Animals grown on plates containing ethanol and DMSO were used as a control for colchicine and Taxol treatment, respectively. Parental (P0) worms were grown from the L4 stage on plates containing drug, and their filial 1 (F1) progeny were scored.

Image acquisition using a point-scanning confocal microscope for the measurement of touch neuron length

Imaging of the neurons, including PLM/ALM and PVD, was performed using a Zeiss Axio Observer LSM 510 Meta confocal microscope. The *Pmec-7*-GFP (*muIs32*) reporter was imaged using 66% of a 488-nm laser, while the *Pmec-4*-mCherry (*tbIs222*) and *Pmec-4*-mScarlet (*shrEx143*) reporters were imaged using 69% of a 543-nm laser under a 40× oil objective (NA 1.3). PVD neurons expressing *PF49H12.4*::GFP+*unc-119* (*wdIs52*) were imaged using a 63× oil objective (NA 1.4). PLM or ALM neurons were imaged at the L4 stage, and PVD neurons were imaged at day 1 adult. Other acquisition parameters included scanning at 1 Airy unit with a 0.62-µm × 0.62-µm × 0.5-µm voxel size, 3.2-µs pixel dwell time, and 4× Kalman averaging. For the normalization of neurite length with respect to body growth, differential interference contrast images were obtained simultaneously with the fluorescence images.

Analysis of PLM process length

The absolute length of the anterior and posterior processes was calculated using the length measurement tool in Zeiss LSM Image Browser software. Segmented traces were drawn along the length of the anterior or posterior process to get the value of length. To avoid the artifact due to the possible defect in body growth, we normalized the anterior process length with the distance between the PLM cell body and the vulva of the respective worm measured from the differential interference contrast image (Fig. 1, A, E, and F). Similarly, we normalized the posterior process length with respect to the distance between the PLM cell body and the tip of the tail. This approach was used in earlier work on TRNs (Lockhead et al., 2016).

Image acquisition and quantification of GFP::PTRN-1 punctae

The worms coexpressing *Pmec-4*-GFP::PTRN-1 (*juEx6455*) and *Pmec-4::mCherry* (*tbIs222*) were immobilized using 10 mM levamisole and imaged with 2% of 488-nm and 0.2% of 561-nm lasers under a 60× oil objective (NA 1.4) of a Nikon A1HD25 confocal microscope. The ratio image was obtained from the maximum intensity projection of GFP::PTRN-1 to mCherry. Peaks in the line profile of the anterior and posterior processes in the ratio image were quantified using the BAR plugin of ImageJ. The amplitude of peaks above threshold 1 was represented as GFP-PTRN-1 punctae (arrowheads, Fig. S2 E). This value was normalized by the length of the line profile (Fig. S2, E and F).

Image acquisition using Nikon Ti-2 widefield epifluorescence microscope

For the RNAi experiments, we imaged the PLM neuron using the Nikon Ti-2 epifluorescence setup with a 60×/1.40 NA oil objective and an Andor Zyla VSC-02284 camera at gain 4 and 300–900-ms exposure. We collected both the fluorescence and bright-field images (Fig. 6, Fa–c). We analyzed these images by using FIJI ImageJ software for the length measurements (Fig. 6, G and H; and Fig. S3, F and G) using the established approaches (Lockhead et al., 2016).

Time-lapse acquisition of EBP-2::GFP, GFP::PTRN-1, GFP::KLP-7, and GFP::RAB-3 using spinning disk confocal microscopy

Fast time-lapse image acquisition was performed using ZEN 2 Blue software on a Zeiss Observer Z1 microscope equipped with a Yokogawa CSU-XA1 spinning disk confocal head and a Photometric Evolve electron-multiplying charge-coupled device camera. The images were captured in a frame of 120 × 120 μm^2 (512 × 512 $pixels^2$) using either a 100×/1.46 NA or a 63×/1.4 NA objective at a rate of 2.64 frames per second for a total duration of 2 min for EBP2::GFP, GFP::PTRN-1, and GFP::KLP-7 reporters. For the GFP::RAB-3 reporter, the images were captured at 3.19 frames per second for 3 min. The best signal-to-noise ratio during imaging of these reporters was obtained at 350-ms exposure time with 70 EM gain of the camera. For EBP-2::GFP, GFP::PTRN-1, and GFP::KLP-7 reporters, 8.75 mW of a 488-nm excitation laser was used, while GFP::RAB-3 was imaged with 10-mW power.

Analysis of EBP-2::GFP, GFP::PTRN-1, and GFP::KLP-7 dynamics

Kymographs (Fig. 2 B) were generated using the Analyze/Multi Kymograph tool in ImageJ software (https://imagej.nih.gov/ij/) from 30-µm ROIs placed on the PLM process (Fig. 2 A). The horizontal axis of the kymograph is the axon length in micrometers, and the vertical axis is the time in seconds. Typically,

EBP-2::GFP tracks are displayed as diagonal tracks. The ROIs were drawn in the distal-to-proximal direction (toward the cell body). Diagonal tracks moving away from the cell body were annotated as "plus-end-out" microtubules (P; green traces in Fig. 2 B), and the tracks moving toward the cell body were annotated as "minus-end-out" microtubules (M; magenta traces in Fig. 2 B). The fractional polarity of microtubules was quantified from the relative number of plus-end-out tracks or minus-end-out tracks to the total number of tracks in the EBP kymographs. A similar method was also used for analyzing GFP::PTRN-1 and GFP::KLP-7 kymographs (Figs. 2 G and 9 B). We obtained a net pixel shift in the x and y axes to calculate the growth length and duration, respectively, for the EBP-2::GFP tracks (Fig. 2, E and F). For the presentation of the movement events of GFP-KLP-7 (Video 3), we drew traces on all the real tracks recognized in a given kymograph and placed an illustrative version of the kymograph next to the real kymograph (e.g., Fig. 9 B).

Analysis of GFP::RAB3 dynamics

Kymographs for GFP::RAB-3 movement (Fig. 2 I) were generated in a similar manner from 30-µm ROIs placed on the PLM process (Fig. 2 A). Typical GFP::RAB-3 tracks are displayed as diagonal tracks (green dotted traces for anterograde tracks and magenta dotted traces for retrograde tracks in Fig. 2 I). The ROIs were drawn in the distal-to-proximal direction (toward the cell body). From each kymograph, anterograde and retrograde RAB-3 particle movement was quantified by calculating a number of tracks in either the anterograde or retrograde direction per 30-µm of length (in micrometers) of axons during the 3 min of image acquisition. The perpendicular tracks (white arrowheads in Fig. 2 I) were considered to be particles that were static during the course of imaging. In some cases, due to the movement of the worm, the axon also moved during the span of imaging. In such situations, we used the Registration/StackReg plugin of ImageJ software to move the ROI along with the axon in the frames when the movement was encountered. When large movement was noticed, we did not consider those movies for further analysis. We obtained a net pixel shift in the x and y axes to calculate the run length and duration, respectively, in the anterograde or retrograde direction. The velocity of the RAB-3 movements was calculated by dividing the pixel shift in the x axis by that in the y axis for a given track according to a method established previously (Mondal et al., 2011).

Intensity measurement and quantification of GFP::KLP-7

The worms coexpressing *Pmec-4*-GFP::KLP-7B (*shrEX127*) and *Pmec-4*::mScarlet (*shrEX143*) were immobilized using 0.1-µm diameter polystyrene beads (Polysciences; 00876-15). GFP::KLP-7B and mScarlet (constitutive reporter) were imaged with 60.5% of 488-nm and 43.6% of 543-nm lasers, respectively, under a 63× oil objective (NA 1.4) of a Zeiss LSM 510 Meta confocal microscope. Average GFP::KLP-7B and mScarlet intensities were measured from a 30-µm ROI (Fig. S3, A and B) from anterior and posterior processes. For background corrections, similar ROIs were also placed outside the PLM neuron to get the intensities of the background.

Image acquisition and quantification for NMY-2::GFP and P*pak*-1:PAK-1:GFP

The worms coexpressing either *Ppak-1*:PAK-1:GFP (*ShrEx439*) or *Pnmy-2*:NMY-2::GFP (*zuIs45*) and *Pmec-4*::mCherry (*tbIs222*) were immobilized using 10 mM levamisole and imaged with 7% of 488-nm and 0.3% of 561-nm lasers under a 60× oil objective (NA 1.4) of a Nikon A1HD25 confocal microscope. Both PAK-1 and NMY-2 are expressed in multiple cells, including touch neurons (Fig. S4, A and B; and Fig. S3 E), making it difficult to see the spatial localization of the reporters within the PLM. To observe PLM neuron-specific localization of PAK-1::GFP or NMY-2::GFP, green channel images (PAK-1:GFP or NMY2::GFP) are processed using the red channel (*Pmec-4*:mCherry). Using ImageJ, the green and red channels were separated, and a binary mask of the red channel was created by thresholding. The resultant image of the AND function between green and binary red was subtracted from the green channel, and the resultant image was again subtracted from the green channel. Representative images are shown in Fig. 6 D for NMY-2GFP (raw image in Fig. S3 E) and are shown for *Ppak-1*::PAK-1::GFP in Fig. 7 B (raw image in Fig. S4, A and B). Line scan plots for GFP and mCherry intensities were measured from 30-µm ROIs from anterior and posterior processes (Figs. 6 D and 7 B). Similar ROIs were also placed outside the PLM neuron to get the intensities of the background.

Immunostaining and analysis

To observe the localization of KLP-7 and ROCK/LET-502, we used the rabbit anti–KLP-7 antibody (Oegema et al., 2001; at 1:500 dilution) and the rat anti–LET-502 antibody (Piekny and Mains, 2002; at 1:500 dilution), respectively. For detecting active PAK-1, we used the rabbit polyclonal antibody against phospho-PAK-1(Thr423; 2601; Cell Signaling Technology; Verboon et al., 2020) at 1:1,000 dilution. We detected the touch neurons expressing *Pmec-7*:GFP using an anti-GFP primary antibody (mAb 3E6, A-11120; Thermo Fisher Scientific) at 1:1,000 dilution. Secondary antibodies were from Molecular Probes (Alexa Fluor 488 [A11001, Texas Red [T6392], and Alexa Fluor 594 [A11012]). Whole-mount immunostaining of worms was done as per a previously described method (Finney and Ruvkun, 1990). We fixed the worms using 1% PFA for 20 min at RT. We incubated the fixed samples in 1% β-mercaptoethanol for 15 min at RT to reduce cuticle cross-links. We performed imaging using a Nikon A1 HD25 laser scanning confocal microscope. Green and red fluorescence was visualized using 1.5% of a 488-nm laser and 0.9% of a 561-nm laser, respectively. Both KLP-7 and PAK-1 are localized in multiple cells, including touch neurons (Figs. S1 F and S4 C), making it difficult to visualize the spatial distribution of the antigens in the PLM neuron. For TRN-specific visualization of the antigen in the immunostained preparations, we processed the images with a TRN binary mask as described in the previous Materials and methods subsection.

Sample preparation, imaging, and analysis of proximity ligation assay (PLA)

We performed the PLA (Chen et al., 2013; Day et al., 2020) using Duolink In Situ Red Starter Kit (Mouse/Rabbit DUO92101;

Sigma-Aldrich) to analyze the in vivo interaction between KLP-7 and PAK-1::GFP in worms expressing the *Ppak-1::pak-1::gfp* reporter (Zhang et al., 2011). L4 stage worms were fixed using 1% PFA for 1 h at RT. To reduce cuticle cross-links, the fixed samples were incubated in 1% β-mercaptoethanol for 40 min at RT (Finney and Ruvkun, 1990). Then the samples were incubated in 1.5% BSA, 1.5% normal goat serum, 0.5% Triton X-100, and 0.05% sodium azide for 1 h at RT for blocking. We used a rabbit anti–KLP-7 antibody (Oegema et al., 2001) at 1:500 dilution and mouse anti-GFP at 1:1,000 dilution (GFP mAb 3E6, A-11120; Invitrogen) for recognizing KLP-7 and PAK-1::GFP, respectively, in the PLA reaction. The sample was incubated with primary antibodies at 4°C overnight with gentle shaking. As per the manufacturer's instructions and a previously described protocol (Day et al., 2020), PLA probes (PLUS and MINUS probes diluted 1:5 with antibody diluent; Sigma-Aldrich) was added to samples and incubated for 1 h at 37°C. For ligation reactions, samples were incubated in ligation solution for 30 min at 37°C, and to detect protein interactions, an amplification solution containing red fluorophores was added to the samples and incubated for 1 h 40 min at 37°C. Then the samples were covered with aluminum foil to protect them from light until mounting using mounting media provided in the PLA kit. We determined the antibody dilutions for the PLA reaction on the basis of dilutions used in the immunostaining experiments to detect KLP-7 (Fig. S1 F) and PAK::GFP (Fig. 7 D) using anti–KLP-7 and anti-GFP, respectively. The PLA samples were imaged in the same way as other immunostained preparations imaged in this study with PLA probe (red) using a 561-nm laser and PAK-1::GFP (green) using a 488-nm laser. As PAK-1::GFP was observable in PLM distinctly (Fig. S4, A and B), we processed the PLA images (Fig. 7 D) using a green channel binary mask as described earlier in the Materials and methods section. Ratio images of the PLA channel to the respective green channel were used to score these foci with the Plot profile function of ImageJ at a threshold of 0.5 (Fig. 7 E). As a control, we performed PLA reactions on worms expressing P*mec-7*-GFP (*muIs32*) with the same antibodies (anti–KLP-7 and anti-GFP), which did not show any PLA signal (Fig. 7 E).

Statistical analysis

All the statistical analyses were performed using GraphPad Prism software version 9.0.2. Each bar in the plots represented the mean value and the SEM. For comparing the proportions, the χ^2 test (Fisher's exact test) was used. For comparing more than two groups, ANOVA was used with a post hoc Tukey's multiple comparisons test. Before proceeding with ANOVA, Bartlett's test for homogeneity of variances was used to test that variances were equal for all samples. In the *klp-7* mutant, the fraction polarity values of microtubules did not follow a normal distribution for the posterior process of the PLM neuron (Fig. 2 C, red arrowheads representing segregation of values). In those cases, the frequency distribution of microtubule polarity was presented (Fig. S2, A–D; Fig. S5, A and B; and Fig. S5, J and K), which made this dispersion clear. In the WT background, the fraction of microtubule with plus-end-out polarity showed a normal distribution with a modal value of 0.5 (asterisk, Fig. S2 C) for the posterior processes, whereas in *klp-7(0)*, there were two mode values of 1 and 0 (asterisk, Fig. S2 C). P values as a measure of significance are represented in the image panels for the respective compared groups. For each bar graph, the sample number (*n*) is presented in the respective figure legend. The *n* values for each bar are the total sample values accumulated over the total number of biological replicates (*N*) in a given experiment.

Online supplemental material

Fig. S1 shows a neuronal phenotype due to microtubule drug treatment or loss of *klp-7*, related to Fig. 1. Fig. S2 shows the changes in microtubule organization and axonal transport in the *klp-7* mutant, related to Fig. 2. Fig. S3 shows the regulation of *klp-7* by the PCP components of Wnt signaling in the PLM neuron, related to Fig. 6. Fig. S4 shows that the *unc-73/ced-10* pathway negatively regulates *klp-7* for the extension of the anterior process of the PLM, related to Fig. 7. Fig. S5 shows regulation of microtubule polarity through Wnt PCP components, related to Fig. 8. Video 1 shows EBP-2::GFP in various genetic backgrounds and is related to Figs. 2, 4, and 5. Video 2 shows GFP::RAB-3 in various genetic backgrounds and is related to Figs. 2, 4, and 5. Video 3 shows the dynamics of the GFP-tagged version of WT KLP-7 and mutant KLP-7$^{S546E\ S555E}$ and is related to Fig. 9. Table S1 shows the phenotype in TRNs in mutants affecting microtubule dynamics. Table S2 shows the results of analysis of the number of EBP-2::GFP tracks in various experiments. Table S3 shows the results of analysis of the growth rate of EBP-2::GFP tracks in PLM neurons. Table S4 lists the *C. elegans* strains used in this study. Table S5 lists strains carrying newly generated extrachromosomal transgenes.

Acknowledgments

We thank Yuji Kohara for cDNAs. We thank the National Bio-Resource Project, Japan, and the *Caenorhabditis* Genetics Center for strains. We thank Arnab Mukhopadhyay, Sandhya Koushika, Sachin Kotak, Marian Chuang, Lizhen Chen, Yishi Jin, Andrew Chisholm, Michael Nonet, Cori Bargmann, Michel Labouesse, Alisa Piekny, and Arshad Desai for help with strains, plasmids, and antibodies. We thank Prerna Srivastava for CRISPR.

This work was supported by the National Brain Research Centre core fund from the Department of Biotechnology, The Wellcome Trust DBT India Alliance (IA/I/13/1/500874), to A. Ghosh-Roy, and by The Wellcome Trust DBT India Alliance early career fellowship (IA/E/18/1/504331) to S. Dey. The *Caenorhabditis* Genetics Center is supported by the National Institutes of Health Office of Research Infrastructure Programs (P40 OD010440).

The authors declare no competing financial interests.

Author contributions: D. Puri, K. Ponniah, and A. Ghosh-Roy designed experiments. D. Puri, K. Ponniah, K. Biswas, and A. Basu performed experiments and analyzed data. A. Ghosh-Roy and D. Puri wrote the manuscript. D. Puri generated reagents; performed point-scanning confocal microscopy of GFP::PTRN-1, GFP::KLP-7, GFP::LET502, PAK-1::GFP, and NMY-2::GFP reporters; performed live imaging of EBP-2::GFP, GFP::PTRN-1, GFP::KLP-7, and GFP::RAB-3 reporters using a spinning disk

confocal microscope; and performed immunohistochemistry, PLA, and drug treatments. K. Biswas performed live imaging of EBP-2::GFP. A. Basu performed live imaging of GFP::RAB-3. K. Ponniah performed crosses, cloning, mutagenesis, and RNAi. S. Dey performed the image analysis of PAK-1::GFP, NMY-2::GFP reporters, and immunostaining data. E.A. Lundquist provided reagents to manipulate small GTPases.

This research was funded in whole or in part by the Wellcome Trust. For the purpose of Open Access, the author has applied a CC-BY public copyright license to any Author Accepted Manuscript (AAM) version arising from this submission.

References

Ackley, B.D. 2014. Wnt-signaling and planar cell polarity genes regulate axon guidance along the anteroposterior axis in *C. elegans*. *Dev. Neurobiol.* 74: 781–796. https://doi.org/10.1002/dneu.22146

Akhmanova, A., and C.C. Hoogenraad. 2015. Microtubule minus-end-targeting proteins. *Curr. Biol.* 25:R162–R171. https://doi.org/10.1016/j.cub.2014.12.027

Alan, J.K., and E.A. Lundquist. 2012. Analysis of Rho GTPase function in axon pathfinding using *Caenorhabditis elegans*. *Methods Mol. Biol.* 827:339–358. https://doi.org/10.1007/978-1-61779-442-1_22

Arimura, N., C. Menager, Y. Fukata, and K. Kaibuchi. 2004. Role of CRMP-2 in neuronal polarity. *J. Neurobiol.* 58:34–47. https://doi.org/10.1002/neu.10269

Baas, P.W., J.S. Deitch, M.M. Black, and G.A. Banker. 1988. Polarity orientation of microtubules in hippocampal neurons: uniformity in the axon and nonuniformity in the dendrite. *Proc. Natl. Acad. Sci. USA.* 85: 8335–8339. https://doi.org/10.1073/pnas.85.21.8335

Basu, A., S. Dey, D. Puri, N. Das Saha, V. Sabharwal, P. Thyagarajan, P. Srivastava, S.P. Koushika, and A. Ghosh-Roy. 2017. *let-7* miRNA controls CED-7 homotypic adhesion and EFF-1-mediated axonal self-fusion to restore touch sensation following injury. *Proc. Natl. Acad. Sci. USA.* 114: E10206–E10215. https://doi.org/10.1073/pnas.1704372114

Bounoutas, A., and M. Chalfie. 2007. Touch sensitivity in *Caenorhabditis elegans*. *Pflugers Arch.* 454:691–702. https://doi.org/10.1007/s00424-006-0187-x

Brenner, S. 1974. The genetics of *Caenorhabditis elegans*. *Genetics.* 77:71–94. https://doi.org/10.1093/genetics/77.1.71

Čajánek, L., R.S. Ganji, C. Henriques-Oliveira, S. Theofilopoulos, P. Koník, V. Bryja, and E. Arenas. 2013. Tiam1 regulates the Wnt/Dvl/Rac1 signaling pathway and the differentiation of midbrain dopaminergic neurons. *Mol. Cell. Biol.* 33:59–70. https://doi.org/10.1128/MCB.00745-12

Cao, Y., J. Lipka, R. Stucchi, M. Burute, X. Pan, S. Portegies, R. Tas, J. Willems, L. Will, H. MacGillavry, et al. 2020. Microtubule minus-end binding protein CAMSAP2 and Kinesin-14 motor KIFC3 control dendritic microtubule organization. *Curr. Biol.* 30:899–908.e6. https://doi.org/10.1016/j.cub.2019.12.056

Chalfie, M., and J.N. Thomson. 1982. Structural and functional diversity in the neuronal microtubules of *Caenorhabditis elegans*. *J. Cell Biol.* 93:15–23. https://doi.org/10.1083/jcb.93.1.15

Chen, S.Y., P.H. Huang, and H.J. Cheng. 2011. Disrupted-in-Schizophrenia 1-mediated axon guidance involves TRIO-RAC-PAK small GTPase pathway signaling. *Proc. Natl. Acad. Sci. USA.* 108:5861–5866. https://doi.org/10.1073/pnas.1018128108

Chen, T.C., Y.W. Liu, Y.H. Huang, Y.C. Yeh, T.Y. Chou, Y.C. Wu, C.C. Wu, Y.R. Chen, H.C. Cheng, P.J. Lu, et al. 2013. Protein phosphorylation profiling using an in situ proximity ligation assay: phosphorylation of AURKA-elicited EGFR-Thr654 and EGFR-Ser1046 in lung cancer cells. *PLoS One.* 8:e55657. https://doi.org/10.1371/journal.pone.0055657

Chuang, M., A. Goncharov, S. Wang, K. Oegema, Y. Jin, and A.D. Chisholm. 2014. The microtubule minus-end-binding protein patronin/PTRN-1 is required for axon regeneration in *C. elegans*. *Cell Rep.* 9:874–883. https://doi.org/10.1016/j.celrep.2014.09.054

Ciani, L., O. Krylova, M.J. Smalley, T.C. Dale, and P.C. Salinas. 2004. A divergent canonical WNT-signaling pathway regulates microtubule dynamics: Dishevelled signals locally to stabilize microtubules. *J. Cell Biol.* 164:243–253. https://doi.org/10.1083/jcb.200309096

Cueva, J.G., J. Hsin, K.C. Huang, and M.B. Goodman. 2012. Posttranslational acetylation of α-tubulin constrains protofilament number in native microtubules. *Curr. Biol.* 22:1066–1074. https://doi.org/10.1016/j.cub.2012.05.012

Day, N.J., X. Wang, and E. Voronina. 2020. In situ detection of ribonucleoprotein complex assembly in the *C. elegans* germline using proximity ligation assay. J. Vis. Exp. (159):e60982. https://doi.org/10.3791/60982

Desai, A., S. Verma, T.J. Mitchison, and C.E. Walczak. 1999. Kin I kinesins are microtubule-destabilizing enzymes. *Cell.* 96:69–78. https://doi.org/10.1016/S0092-8674(00)80960-5

Domnitz, S.B., M. Wagenbach, J. Decarreau, and L. Wordeman. 2012. MCAK activity at microtubule tips regulates spindle microtubule length to promote robust kinetochore attachment. *J. Cell Biol.* 197:231–237. https://doi.org/10.1083/jcb.201108147

Ems-McClung, S.C., S.G. Hainline, J. Devare, H. Zong, S. Cai, S.K. Carnes, S.L. Shaw, and C.E. Walczak. 2013. Aurora B inhibits MCAK activity through a phosphoconformational switch that reduces microtubule association. *Curr. Biol.* 23:2491–2499. https://doi.org/10.1016/j.cub.2013.10.054

Feng, C., P. Thyagarajan, M. Shorey, D.Y. Seebold, A.T. Weiner, R.M. Albertson, K.S. Rao, A. Sagasti, D.J. Goetschius, and M.M. Rolls. 2019. Patronin-mediated minus end growth is required for dendritic microtubule polarity. *J. Cell Biol.* 218:2309–2328. https://doi.org/10.1083/jcb.201810155

Finney, M., and G. Ruvkun. 1990. The unc-86 gene product couples cell lineage and cell identity in *C. elegans*. *Cell.* 63:895–905. https://doi.org/10.1016/0092-8674(90)90493-X

Friedland, A.E., Y.B. Tzur, K.M. Esvelt, M.P. Colaiácovo, G.M. Church, and J.A. Calarco. 2013. Heritable genome editing in *C. elegans* via a CRISPR-Cas9 system. *Nat. Methods.* 10:741–743. https://doi.org/10.1038/nmeth.2532

Ghosh-Roy, A., A. Goncharov, Y. Jin, and A.D. Chisholm. 2012. Kinesin-13 and tubulin posttranslational modifications regulate microtubule growth in axon regeneration. *Dev. Cell.* 23:716–728. https://doi.org/10.1016/j.devcel.2012.08.010

Gönczy, P., S. Pichler, M. Kirkham, and A.A. Hyman. 1999. Cytoplasmic dynein is required for distinct aspects of MTOC positioning, including centrosome separation, in the one cell stage *Caenorhabditis elegans* embryo. *J. Cell Biol.* 147:135–150. https://doi.org/10.1083/jcb.147.1.135

Greer, Y.E., and J.S. Rubin. 2011. Casein kinase 1 delta functions at the centrosome to mediate Wnt-3a-dependent neurite outgrowth. *J. Cell Biol.* 192:993–1004. https://doi.org/10.1083/jcb.201011111

Habas, R., I.B. Dawid, and X. He. 2003. Coactivation of Rac and Rho by Wnt/Frizzled signaling is required for vertebrate gastrulation. *Genes Dev.* 17: 295–309. https://doi.org/10.1101/gad.1022203

Harterink, M., S.L. Edwards, B. de Haan, K.W. Yau, S. van den Heuvel, L.C. Kapitein, K.G. Miller, and C.C. Hoogenraad. 2018. Local microtubule organization promotes cargo transport in *C. elegans* dendrites. *J. Cell Sci.* 131:jcs223107. https://doi.org/10.1242/jcs.223107

Helenius, J., G. Brouhard, Y. Kalaidzidis, S. Diez, and J. Howard. 2006. The depolymerizing kinesin MCAK uses lattice diffusion to rapidly target microtubule ends. *Nature.* 441:115–119. https://doi.org/10.1038/nature04736

Hilliard, M.A., and C.I. Bargmann. 2006. Wnt signals and Frizzled activity orient anterior-posterior axon outgrowth in *C. elegans*. *Dev. Cell.* 10: 379–390. https://doi.org/10.1016/j.devcel.2006.01.013

Homma, N., Y. Takei, Y. Tanaka, T. Nakata, S. Terada, M. Kikkawa, Y. Noda, and N. Hirokawa. 2003. Kinesin superfamily protein 2A (KIF2A) functions in suppression of collateral branch extension. *Cell.* 114:229–239. https://doi.org/10.1016/S0092-8674(03)00522-1

Homma, N., R. Zhou, M.I. Naseer, A.G. Chaudhary, M.H. Al-Qahtani, and N. Hirokawa. 2018. KIF2A regulates the development of dentate granule cells and postnatal hippocampal wiring. *eLife.* 7:e30935. https://doi.org/10.7554/eLife.30935

Kamath, R.S., M. Martinez-Campos, P. Zipperlen, A.G. Fraser, and J. Ahringer. 2001. Effectiveness of specific RNA-mediated interference through ingested double-stranded RNA in *Caenorhabditis elegans*. Genome Biol. 2: research0002.

Kapitein, L.C., and C.C. Hoogenraad. 2015. Building the neuronal microtubule cytoskeleton. *Neuron.* 87:492–506. https://doi.org/10.1016/j.neuron.2015.05.046

Kirszenblat, L., B. Neumann, S. Coakley, and M.A. Hilliard. 2013. A dominant mutation in mec-7/β-tubulin affects axon development and regeneration in *Caenorhabditis elegans* neurons. *Mol. Biol. Cell.* 24:285–296. https://doi.org/10.1091/mbc.e12-06-0441

Komarova, Y.A., I.A. Vorobjev, and G.G. Borisy. 2002. Life cycle of MTs: persistent growth in the cell interior, asymmetric transition frequencies and effects of the cell boundary. *J. Cell Sci.* 115:3527–3539. https://doi.org/10.1242/jcs.115.17.3527

Leterrier, C., H. Vacher, M.P. Fache, S.A. d'Ortoli, F. Castets, A. Autillo-Touati, and B. Dargent. 2011. End-binding proteins EB3 and EB1 link

microtubules to ankyrin G in the axon initial segment. *Proc. Natl. Acad. Sci. USA.* 108:8826–8831. https://doi.org/10.1073/pnas.1018671108

Levy-Strumpf, N., M. Krizus, H. Zheng, L. Brown, and J.G. Culotti. 2015. The Wnt Frizzled receptor MOM-5 regulates the UNC-5 netrin receptor through small GTPase-dependent signaling to determine the polarity of migrating cells. *PLoS Genet.* 11:e1005446. https://doi.org/10.1371/journal.pgen.1005446

Liang, X., M. Kokes, R.D. Fetter, M.D. Sallee, A.W. Moore, J.L. Feldman, and K. Shen. 2020. Growth cone-localized microtubule organizing center establishes microtubule orientation in dendrites. *eLife.* 9:e56547. https://doi.org/10.7554/eLife.56547

Liu, Y., J. Shi, C.C. Lu, Z.B. Wang, A.I. Lyuksyutova, X.J. Song, and Y. Zou. 2005. Ryk-mediated Wnt repulsion regulates posterior-directed growth of corticospinal tract. *Nat. Neurosci.* 8:1151–1159. https://doi.org/10.1038/nn1520

Lockhead, D., E.M. Schwarz, R. O'Hagan, S. Bellotti, M. Krieg, M.M. Barr, A.R. Dunn, P.W. Sternberg, and M.B. Goodman. 2016. The tubulin repertoire of *Caenorhabditis elegans* sensory neurons and its context-dependent role in process outgrowth. *Mol. Biol. Cell.* 27:3717–3728. https://doi.org/10.1091/mbc.e16-06-0473

Lumpkin, E.A., K.L. Marshall, and A.M. Nelson. 2010. The cell biology of touch. *J. Cell Biol.* 191:237–248. https://doi.org/10.1083/jcb.201006074

Lyuksyutova, A.I., C.C. Lu, N. Milanesio, L.A. King, N. Guo, Y. Wang, J. Nathans, M. Tessier-Lavigne, and Y. Zou. 2003. Anterior-posterior guidance of commissural axons by Wnt-Frizzled signaling. *Science.* 302:1984–1988. https://doi.org/10.1126/science.1089610

Maeder, C.I., K. Shen, and C.C. Hoogenraad. 2014. Axon and dendritic trafficking. *Curr. Opin. Neurobiol.* 27:165–170. https://doi.org/10.1016/j.conb.2014.03.015

Maniar, T.A., M. Kaplan, G.J. Wang, K. Shen, L. Wei, J.E. Shaw, S.P. Koushika, and C.I. Bargmann. 2012. UNC-33 (CRMP) and ankyrin organize microtubules and localize kinesin to polarize axon-dendrite sorting. *Nat. Neurosci.* 15:48–56. https://doi.org/10.1038/nn.2970

Michaux, J.B., F.B. Robin, W.M. McFadden, and E.M. Munro. 2018. Excitable RhoA dynamics drive pulsed contractions in the early *C. elegans* embryo. *J. Cell Biol.* 217:4230–4252. https://doi.org/10.1083/jcb.201806161

Mitchison, T., and M. Kirschner. 1984. Dynamic instability of microtubule growth. *Nature.* 312:237–242. https://doi.org/10.1038/312237a0

Mondal, S., S. Ahlawat, K. Rau, V. Venkataraman, and S.P. Koushika. 2011. Imaging in vivo neuronal transport in genetic model organisms using microfluidic devices. *Traffic.* 12:372–385. https://doi.org/10.1111/j.1600-0854.2010.01157.x

Nakata, T., and N. Hirokawa. 2003. Microtubules provide directional cues for polarized axonal transport through interaction with kinesin motor head. *J. Cell Biol.* 162:1045–1055. https://doi.org/10.1083/jcb.200302175

Nance, J., E.M. Munro, and J.R. Priess. 2003. *C. elegans* PAR-3 and PAR-6 are required for apicobasal asymmetries associated with cell adhesion and gastrulation. *Development.* 130:5339–5350. https://doi.org/10.1242/dev.00735

Newsome, T.P., S. Schmidt, G. Dietzl, K. Keleman, B. Asling, A. Debant, and B.J. Dickson. 2000. Trio combines with dock to regulate Pak activity during photoreceptor axon pathfinding in *Drosophila*. *Cell.* 101:283–294. https://doi.org/10.1016/S0092-8674(00)80838-7

Norris, A.D., L. Sundararajan, D.E. Morgan, Z.J. Roberts, and E.A. Lundquist. 2014. The UNC-6/Netrin receptors UNC-40/DCC and UNC-5 inhibit growth cone filopodial protrusion via UNC-73/Trio, Rac-like GTPases and UNC-33/CRMP. *Development.* 141:4395–4405. https://doi.org/10.1242/dev.110437

Oegema, K., A. Desai, S. Rybina, M. Kirkham, and A.A. Hyman. 2001. Functional analysis of kinetochore assembly in *Caenorhabditis elegans*. *J. Cell Biol.* 153:1209–1226. https://doi.org/10.1083/jcb.153.6.1209

Ogawa, T., and N. Hirokawa. 2015. Microtubule destabilizer KIF2A undergoes distinct site-specific phosphorylation cascades that differentially affect neuronal morphogenesis. *Cell Rep.* 12:1774–1788. https://doi.org/10.1016/j.celrep.2015.08.018

Ogawa, T., S. Saijo, N. Shimizu, X. Jiang, and N. Hirokawa. 2017. Mechanism of catalytic microtubule depolymerization via KIF2-tubulin transitional conformation. *Cell Rep.* 20:2626–2638. https://doi.org/10.1016/j.celrep.2017.08.067

Oguchi, Y., S. Uchimura, T. Ohki, S.V. Mikhailenko, and S. Ishiwata. 2011. The bidirectional depolymerizer MCAK generates force by disassembling both microtubule ends. *Nat. Cell Biol.* 13:846–852. https://doi.org/10.1038/ncb2256

Peris, L., M. Wagenbach, L. Lafanechère, J. Brocard, A.T. Moore, F. Kozielski, D. Job, L. Wordeman, and A. Andrieux. 2009. Motor-dependent microtubule disassembly driven by tubulin tyrosination. *J. Cell Biol.* 185:1159–1166. https://doi.org/10.1083/jcb.200902142

Piekny, A.J., and P.E. Mains. 2002. Rho-binding kinase (LET-502) and myosin phosphatase (MEL-11) regulate cytokinesis in the early *Caenorhabditis elegans* embryo. *J. Cell Sci.* 115:2271–2282. https://doi.org/10.1242/jcs.115.11.2271

Prasad, B.C., and S.G. Clark. 2006. Wnt signaling establishes anteroposterior neuronal polarity and requires retromer in *C. elegans*. *Development.* 133:1757–1766. https://doi.org/10.1242/dev.02357

Purro, S.A., L. Ciani, M. Hoyos-Flight, E. Stamatakou, E. Siomou, and P.C. Salinas. 2008. Wnt regulates axon behavior through changes in microtubule growth directionality: a new role for adenomatous polyposis coli. *J. Neurosci.* 28:8644–8654. https://doi.org/10.1523/JNEUROSCI.2320-08.2008

Ritter, A., M. Sanhaji, A. Friemel, S. Roth, U. Rolle, F. Louwen, and J. Yuan. 2015. Functional analysis of phosphorylation of the mitotic centromere-associated kinesin by Aurora B kinase in human tumor cells. *Cell Cycle.* 14:3755–3767. https://doi.org/10.1080/15384101.2015.1068481

Rolls, M.M. 2011. Neuronal polarity in *Drosophila*: sorting out axons and dendrites. *Dev. Neurobiol.* 71:419–429. https://doi.org/10.1002/dneu.20836

Sarov, M., J.I. Murray, K. Schanze, A. Pozniakovski, W. Niu, K. Angermann, S. Hasse, M. Rupprecht, E. Vinis, M. Tinney, et al. 2012. A genome-scale resource for in vivo tag-based protein function exploration in *C. elegans*. *Cell.* 150:855–866. https://doi.org/10.1016/j.cell.2012.08.001

Schiff, P.B., J. Fant, and S.B. Horwitz. 1979. Promotion of microtubule assembly in vitro by taxol. *Nature.* 277:665–667. https://doi.org/10.1038/277665a0

Schlessinger, K., A. Hall, and N. Tolwinski. 2009. Wnt signaling pathways meet Rho GTPases. *Genes Dev.* 23:265–277. https://doi.org/10.1101/gad.1760809

Shelly, M., B.K. Lim, L. Cancedda, S.C. Heilshorn, H. Gao, and M.M. Poo. 2010. Local and long-range reciprocal regulation of cAMP and cGMP in axon/dendrite formation. *Science.* 327:547–552. https://doi.org/10.1126/science.1179735

Srayko, M., A. Kaya, J. Stamford, and A.A. Hyman. 2005. Identification and characterization of factors required for microtubule growth and nucleation in the early *C. elegans* embryo. *Dev. Cell.* 9:223–236. https://doi.org/10.1016/j.devcel.2005.07.003

Stanganello, E., E.E. Zahavi, M. Burute, J. Smits, I. Jordens, M.M. Maurice, L.C. Kapitein, and C.C. Hoogenraad. 2019. Wnt signaling directs neuronal polarity and axonal growth. *iScience.* 13:318–327. https://doi.org/10.1016/j.isci.2019.02.029

Steven, R., T.J. Kubiseski, H. Zheng, S. Kulkarni, J. Mancillas, A. Ruiz Morales, C.W. Hogue, T. Pawson, and J. Culotti. 1998. UNC-73 activates the Rac GTPase and is required for cell and growth cone migrations in *C. elegans*. *Cell.* 92:785–795. https://doi.org/10.1016/S0092-8674(00)81406-3

Tas, R.P., A. Chazeau, B.M.C. Cloin, M.L.A. Lambers, C.C. Hoogenraad, and L.C. Kapitein. 2017. Differentiation between oppositely oriented microtubules controls polarized neuronal transport. *Neuron.* 96:1264–1271.e5. https://doi.org/10.1016/j.neuron.2017.11.018

Trofimova, D., M. Paydar, A. Zara, L. Talje, B.H. Kwok, and J.S. Allingham. 2018. Ternary complex of Kif2A-bound tandem tubulin heterodimers represents a kinesin-13-mediated microtubule depolymerization reaction intermediate. *Nat. Commun.* 9:2628. https://doi.org/10.1038/s41467-018-05025-7

van Beuningen, S.F., and C.C. Hoogenraad. 2016. Neuronal polarity: remodeling microtubule organization. *Curr. Opin. Neurobiol.* 39:1–7. https://doi.org/10.1016/j.conb.2016.02.003

van Beuningen, S.F.B., L. Will, M. Harterink, A. Chazeau, E.Y. van Battum, C.P. Frias, M.A.M. Franker, E.A. Katrukha, R. Stucchi, K. Vocking, et al. 2015. TRIM46 controls neuronal polarity and axon specification by driving the formation of parallel microtubule arrays. *Neuron.* 88:1208–1226. https://doi.org/10.1016/j.neuron.2015.11.012

Vasudevan, K.K., Y.Y. Jiang, K.F. Lechtreck, Y. Kushida, L.M. Alford, W.S. Sale, T. Hennessey, and J. Gaertig. 2015. Kinesin-13 regulates the quantity and quality of tubulin inside cilia. *Mol. Biol. Cell.* 26:478–494. https://doi.org/10.1091/mbc.E14-09-1354

Verboon, J.M., D. Mahmut, A.R. Kim, M. Nakamura, N.J. Abdulhay, S.K. Nandakumar, N. Gupta, T.E. Akie, A.E. Geddis, B. Manes, et al. 2020. Infantile myelofibrosis and myeloproliferation with CDC42 dysfunction. *J. Clin. Immunol.* 40:554–566. https://doi.org/10.1007/s10875-020-00778-7

Wang, Y., M. Rui, Q. Tang, S. Bu, and F. Yu. 2019. Patronin governs minus-end-out orientation of dendritic microtubules to promote dendrite pruning in *Drosophila*. *eLife.* 8:e39964. https://doi.org/10.7554/eLife.39964

Wernike, D., Y. Chen, K. Mastronardi, N. Makil, and A. Piekny. 2016. Mechanical forces drive neuroblast morphogenesis and are required for epidermal closure. *Dev. Biol.* 412:261–277. https://doi.org/10.1016/j.ydbio.2016.02.023

Witte, H., D. Neukirchen, and F. Bradke. 2008. Microtubule stabilization specifies initial neuronal polarization. *J. Cell Biol.* 180:619–632. https://doi.org/10.1083/jcb.200707042

Yau, K.W., S.F. van Beuningen, I. Cunha-Ferreira, B.M. Cloin, E.Y. van Battum, L. Will, P. Schätzle, R.P. Tas, J. van Krugten, E.A. Katrukha, et al. 2014. Microtubule minus-end binding protein CAMSAP2 controls axon specification and dendrite development. *Neuron.* 82:1058–1073. https://doi.org/10.1016/j.neuron.2014.04.019

Yau, K.W., P. Schätzle, E. Tortosa, S. Pagès, A. Holtmaat, L.C. Kapitein, and C.C. Hoogenraad. 2016. Dendrites in vitro and in vivo contain microtubules of opposite polarity and axon formation correlates with uniform plus-end-out microtubule orientation. *J. Neurosci.* 36:1071–1085. https://doi.org/10.1523/JNEUROSCI.2430-15.2016

Yogev, S., and K. Shen. 2017. Establishing neuronal polarity with environmental and intrinsic mechanisms. *Neuron.* 96:638–650. https://doi.org/10.1016/j.neuron.2017.10.021

Yogev, S., R. Cooper, R. Fetter, M. Horowitz, and K. Shen. 2016. Microtubule organization determines axonal transport dynamics. *Neuron.* 92:449–460. https://doi.org/10.1016/j.neuron.2016.09.036

Yoshimura, T., Y. Kawano, N. Arimura, S. Kawabata, A. Kikuchi, and K. Kaibuchi. 2005. GSK-3beta regulates phosphorylation of CRMP-2 and neuronal polarity. *Cell.* 120:137–149. https://doi.org/10.1016/j.cell.2004.11.012

Zhang, H., F. Landmann, H. Zahreddine, D. Rodriguez, M. Koch, and M. Labouesse. 2011. A tension-induced mechanotransduction pathway promotes epithelial morphogenesis. *Nature.* 471:99–103. https://doi.org/10.1038/nature09765

Zheng, C., M. Diaz-Cuadros, and M. Chalfie. 2015. Dishevelled attenuates the repelling activity of Wnt signaling during neurite outgrowth in *Caenorhabditis elegans*. *Proc. Natl. Acad. Sci. USA.* 112:13243–13248. https://doi.org/10.1073/pnas.1518686112

Zheng, C., M. Diaz-Cuadros, and M. Chalfie. 2016. GEFs and Rac GTPases control directional specificity of neurite extension along the anterior-posterior axis. *Proc. Natl. Acad. Sci. USA.* 113:6973–6978. https://doi.org/10.1073/pnas.1607179113

Zheng, C., M. Diaz-Cuadros, K.C.Q. Nguyen, D.H. Hall, and M. Chalfie. 2017. Distinct effects of tubulin isotype mutations on neurite growth in *Caenorhabditis elegans*. *Mol. Biol. Cell.* 28:2786–2801. https://doi.org/10.1091/mbc.e17-06-0424

Zheng, Q., S. Ahlawat, A. Schaefer, T. Mahoney, S.P. Koushika, and M.L. Nonet. 2014. The vesicle protein SAM-4 regulates the processivity of synaptic vesicle transport. *PLoS Genet.* 10:e1004644.

JCB

Supplemental material

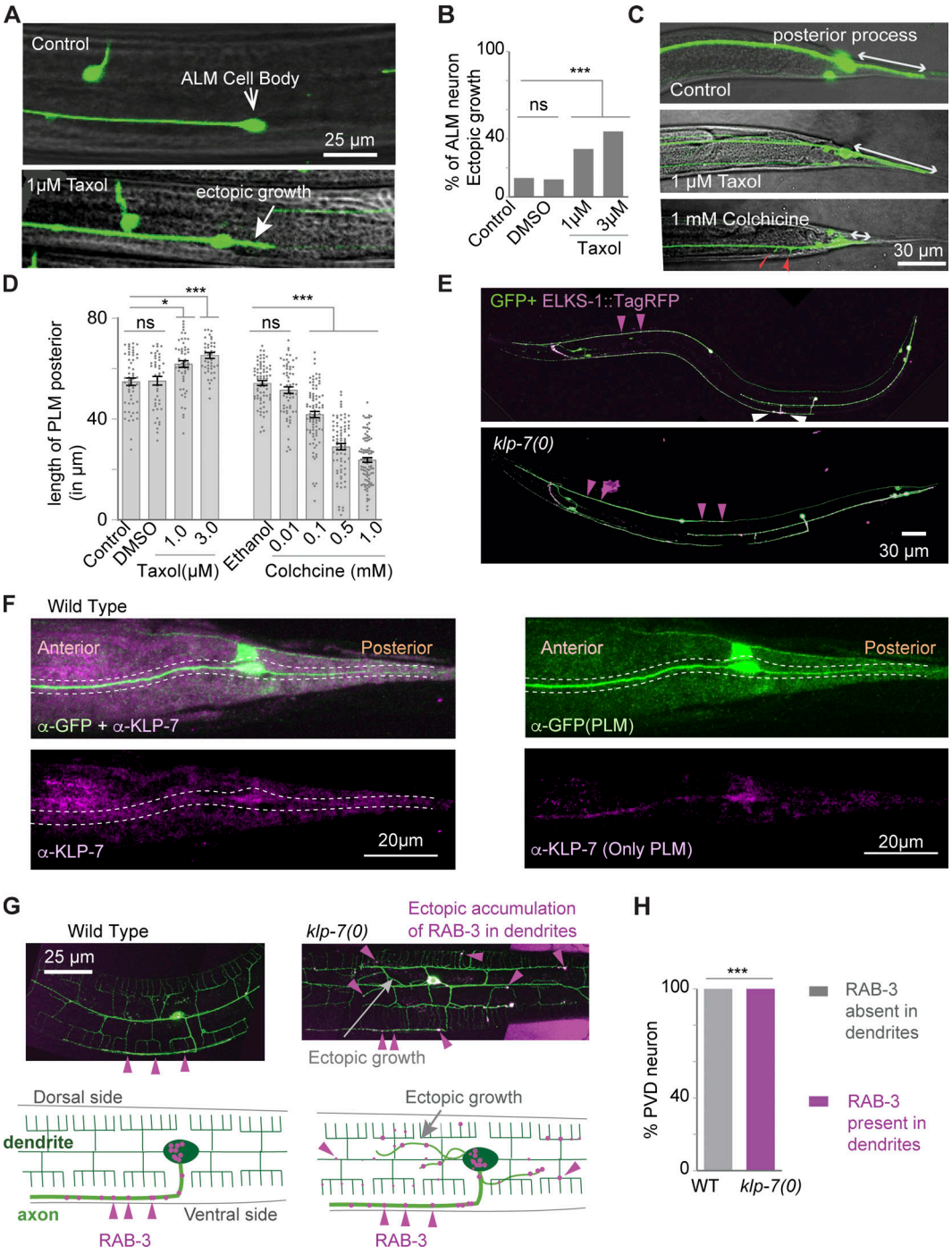

Figure S1. **Neuronal phenotype due to microtubule drug treatment or loss of *klp-7*, related to Fig. 1. (A)** Confocal images of GFP-labeled (*Pmec-7*-GFP, *muIs32*) ALM neuron in untreated and 1 µM Taxol–treated worms. **(B)** The percentage of ALM neurons having ectopic growth due to treatment with different concentrations of Taxol. N = 3 independent replicates; *n* (number of neurons) = 65–142. **(C)** Representative images of PLM neurons in the untreated, 1 µM Taxol–treated, and 1 mM colchicine-treated worms showing the change in the length of the posterior process (double-sided arrow). Red arrowheads show ectopic branches. **(D)** Length of the posterior process of the PLM in worms grown in various concentrations of Taxol and colchicine. N = 3–5 independent replicates; *n* (number of neurons) = 45–95. **(E)** Confocal images of WT and *klp-7(0)* worms expressing *Pmec-7*-TagRFP::ELKS-1 (*jsIs1075*) + P*mec-7*-GFP (*muIs32*). ELKS-1 puncta (magenta arrowheads) were noticed in the axonal and ectopic processes of the ALM. The white arrowheads indicate the enrichment of TagRFP::ELKS-1 at the synaptic region of PLM. **(F)** Confocal images of worms expressing P*mec-7*-GFP (*muIs32*). Worms were immunostained using anti-GFP (shown in green) and anti–KLP-7 (shown in magenta) antibodies. The processed image to visualize the PLM-specific localization of KLP-7 is also presented separately, which is labeled as "α-KLP-7 (Only PLM)." **(G)** Confocal images and schematic of PVD neuron expressing *Pdes-2::mCherry*::RAB-3 (*kyIs445*) and *PF49H124::GFP* (*wdIs52*) reporters. Ectopic outgrowths (arrow) from the cell body and RAB-3 punctae (magenta arrowheads) in the dendrites were noticed in the *klp-7(0)* mutant. **(H)** The percentage of PVD neurons showing ectopic accumulation of mCherry::RAB-3 in dendrites. N = 4–5 independent replicates; *n* (number of neurons) = 25–30. Error bars represent SEM. Statistical comparison was done using the χ^2 (Fisher's exact) test for B and G. ANOVA with Tukey's multiple comparison test was used for D. *, P < 0.05; ***, P < 0.001.

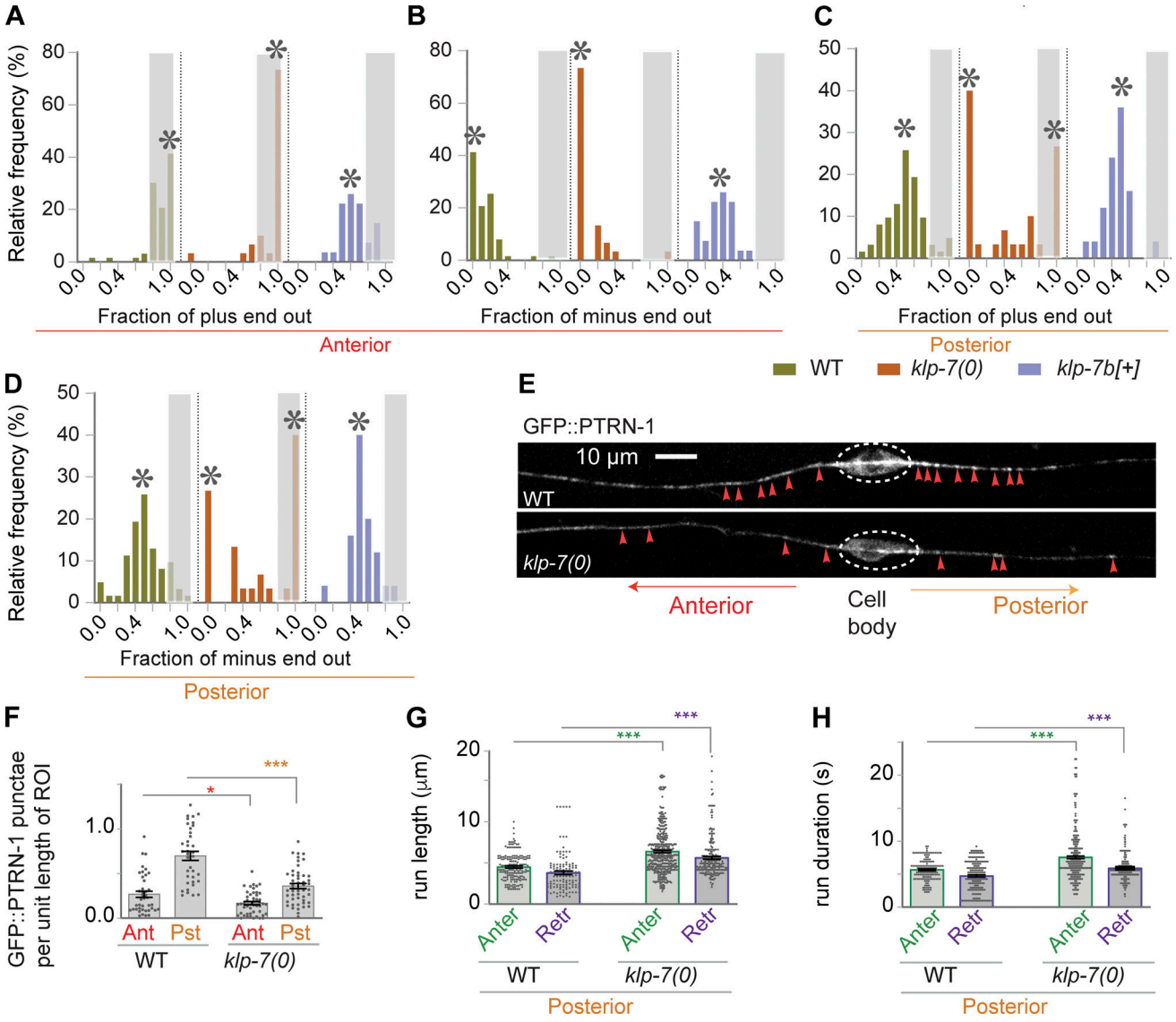

Figure S2. **The changes in microtubule organization and axonal transport in the *klp-7* mutant, related to Fig. 2. (A–D)** Frequency distribution of the fraction polarity values of microtubules with plus-end-out (A and C) or minus-end-out (B and D) polarity in anterior (A and B) and posterior (C and D) processes of the PLM. Asterisks indicate the mode value for each distribution, and the gray shaded areas represent the population of the microtubules having fraction polarity value 0.8 or above. N = 3–8 independent replicates; *n* (number of neurons) = 28–63. **(E)** Confocal images of P*mec-4*-GFP::PTRN-1 (*juEx6455*). Arrowheads indicate the minus end–related enrichment of PTRN-1. **(F)** Quantification of GFP::PTRN-1 punctae per unit length of ROI of the anterior (Ant) and posterior (Pst) processes of the PLM. N = 3–5 independent replicates; *n* (number of neurons) = 37–49. **(G and H)** Histograms depicting length (G) and duration (H) of the GFP::RAB-3 movement events as shown in Fig. 2 I. Anter, anterograde; Retr, retrograde. N = 3–8 independent replicates; *n* (number of GFP::RAB-3 tracks) = 122–452. Error bars represent SEM. Statistical comparisons were done using ANOVA with Tukey's multiple comparison test (F–H). *, P < 0.05; ***, P < 0.001.

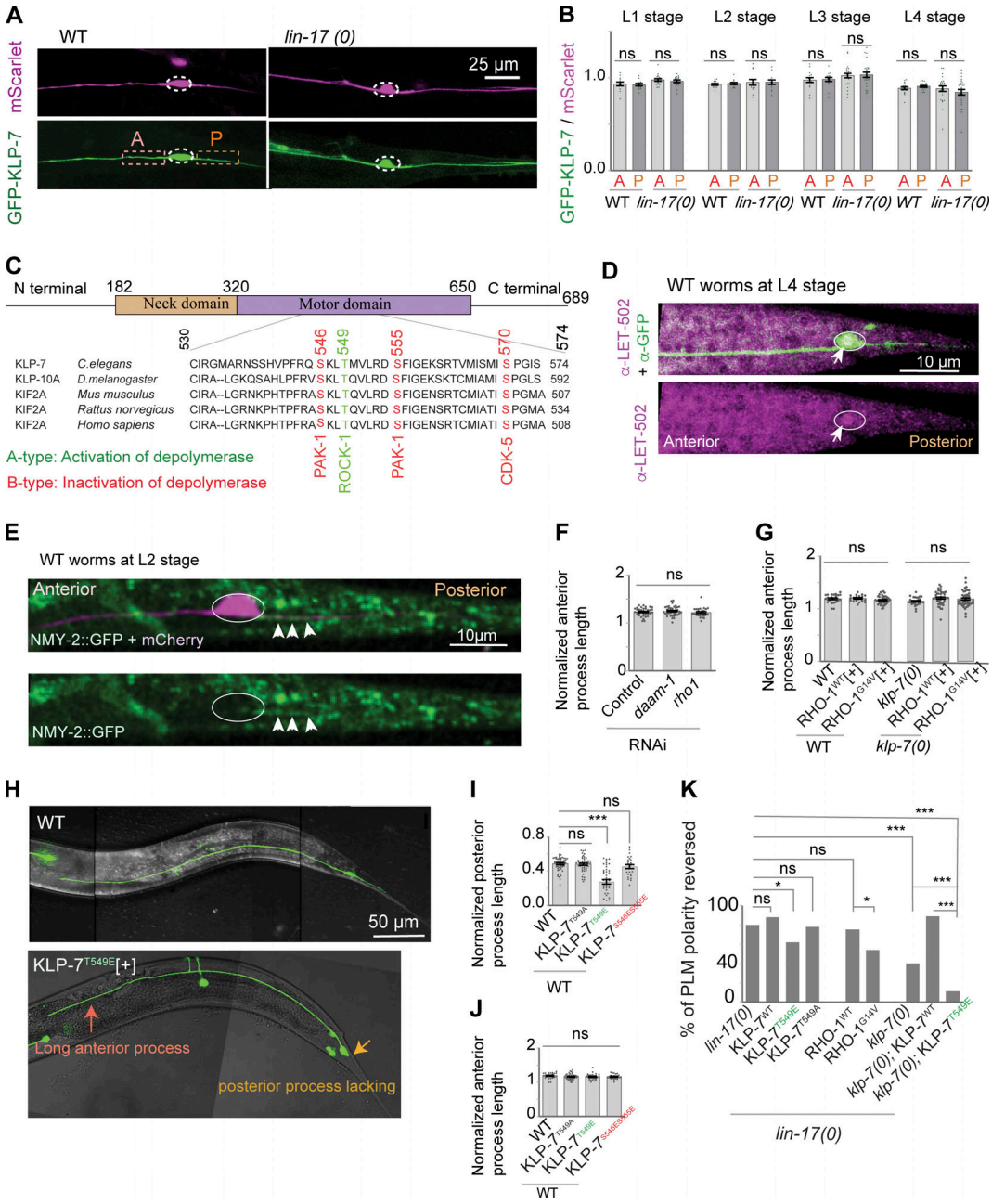

Figure S3. **Regulation of *klp-7* by the PCP components of Wnt signaling in the PLM neuron, related to Fig. 6. (A)** Confocal images of PLM neurons expressing a constitutive marker *Pmec-4::mScarlet* (*shrEx143*; magenta) and *Pmec-4*-GFP::KLP-7B (*shrEx127*; green) in WT and *lin-17(0)* at the L4 stage. **(B)** Histogram showing the normalized GFP::KLP-7 measured from the 30-µm ROIs placed on the anterior (A) and posterior (P) processes of the PLM as shown in A from L1 to L4 stages. N = 3–4 independent replicates; *n* (number of neurons) = 13–25. **(C)** Sequence alignment of the consensus amino acid stretch known to undergo phosphorylation in the neuron in the motor domain of Kinesin-13 homologues in various species. Sites of A-type phosphorylation catalyzed by ROCK (amino acid 549) and B-type phosphorylation catalyzed either by PAK-1 (aa 546 and 555) are highlighted. **(D)** Localization of LET-502 in the PLM (white arrows) using a rat anti–LET-502 antibody (magenta). TRN expressing GFP is stained using an anti-GFP mAb (green). **(E)** Representative image of worms expressing *Pnmy-2*:NMY-2::GFP. Touch neurons are labeled by *tbIs222* (*Pmec-4*:mCherry), and enrichment of NMY-2::GFP in the PLM posterior process is indicated by white arrowheads. **(F)** The normalized length of the anterior process (length of anterior process/distance between PLM cell body and vulva) due to RNAi of *daam-1* or *rho-1*. **(G)** The change in the normalized length of the anterior process due to the overexpression of P*mec-4*-RHO-1^{WT} (*shrEx265*) or a constitutively activated form of RHO-1, P*mec-4*-RHO-1^{G14V} (*shrEx259*). N = 3–8 independent replicates; *n* (number of neurons) = 20–49. **(H)** Overexpression of the A-type phosphorylated version of KLP-7 using P*unc-86*-KLP-7^{T549E} (*shrEx181*) makes a longer anterior process (orange arrow) and shorter posterior process (yellow arrow). **(I and J)** Normalized posterior (I) and anterior (J) lengths of a PLM expressing various mutant forms of KLP-7 in the WT background. *Punc-86*-KLP-7^{T549E} (*shrEx181*) and P*unc-86-4*-KLP-7^{T549A} (*shrEx216*) transgenes were used to express the constitutively phosphorylated and phosphodead versions of KLP-7, respectively. N = 3 independent replicates; *n* (number of neurons) = 22–55. **(K)** Bar chart showing the percentage of PLM neurons with polarity reversal phenotype when various mutant forms of KLP-7 and RHO-1 are overexpressed in *lin-17(0)* or *lin-17(0);klp-7(0)* background. N = 3–4 independent replicates; *n* (number of neurons) = 28–63. Error bars represent SEM. Statistical comparisons were done using ANOVA with Tukey's multiple comparison test (B, D, E, G, and H) or Fisher's exact test (I). *, P < 0.05; ***, P < 0.001.

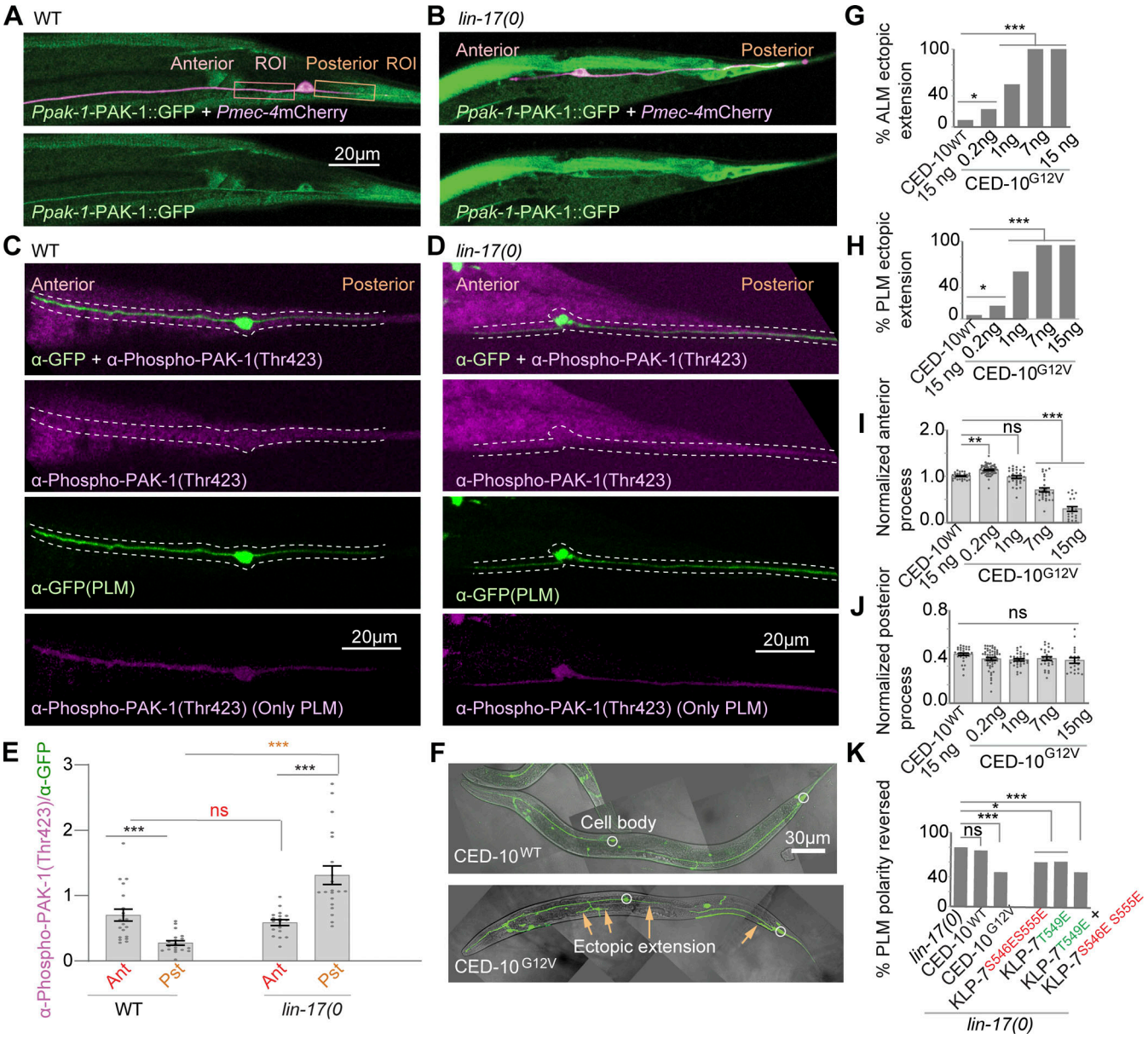

Figure S4. ***unc-73/ced-10* pathway negatively regulates *klp-7* for the extension of the anterior process of the PLM, related to Fig. 7. (A and B)** Confocal images of worms expressing *Ppak-1*:PAK-1::GFP (*shrEx439*) and *Pmec-4*:mCherry in WT (A) and *lin-17(0*; B). **(C and D)** Confocal images of worms expressing P*mec-7*-GFP (*muIs32*). Worms were immunostained using anti–phospho-PAK-1(Thr423; magenta) and anti-GFP (green) antibodies in WT (C) and *lin-17(0*; D). The processed image obtained to visualize the PLM-specific localization of PAK-1 is also presented separately, which is labeled as "α-Phospho-PAK-1(Thr423) (Only PLM)." **(E)** Quantification of fluorescence intensity corresponding to the anti–PAK-1 immunohistochemistry shown in C and D. Ant, anterior; Pst, posterior. **(F)** Confocal images of worms expressing P*mec-7-GFP* (*muIs32*) reporter show that an activated version of CED-10 (CED-10^{G12V}) leads to ectopic extensions from ALM and PLM cell bodies (orange arrows). P*mec-4*-CED-10^{WT} (*shrEx262*) and P*mec-4*-CED-10^{G12V} (*shrEx256*) transgenes were used in this experiment. **(G and H)** The percentage of worms showing ectopic extension phenotype in ALM (G) and PLM (H) neurons. N = 3–4 independent replicates; *n* (number of neurons) = 23–65. **(I and J)** Normalized lengths of anterior (I) and posterior (J) processes of the PLM due to the expression of P*mec-4*-CED-10^{G12V} (*shrEx256*) at various concentrations in the WT background. N = 3–4 independent replicates; *n* (number of neurons) = 20–62. **(K)** The change in the percentage of PLM neurons with polarity reversal phenotype due to expression of either an inactive (B-type) version of KLP-7 (KLP-$7^{S546E\ S555E}$) or an activated version of CED-10 (CED-10^{G12V}) in *lin-17(0)* background. N = 3–4 independent replicates; *n* (number of neurons) = 32–115. Error bars represent SEM. Statistical comparisons were made using the χ^2 (Fisher's exact) test (G, H, and K) and ANOVA with Tukey's multiple comparison test (E, I, and J). *, P < 0.05; **, P < 0.01; ***, P < 0.001.

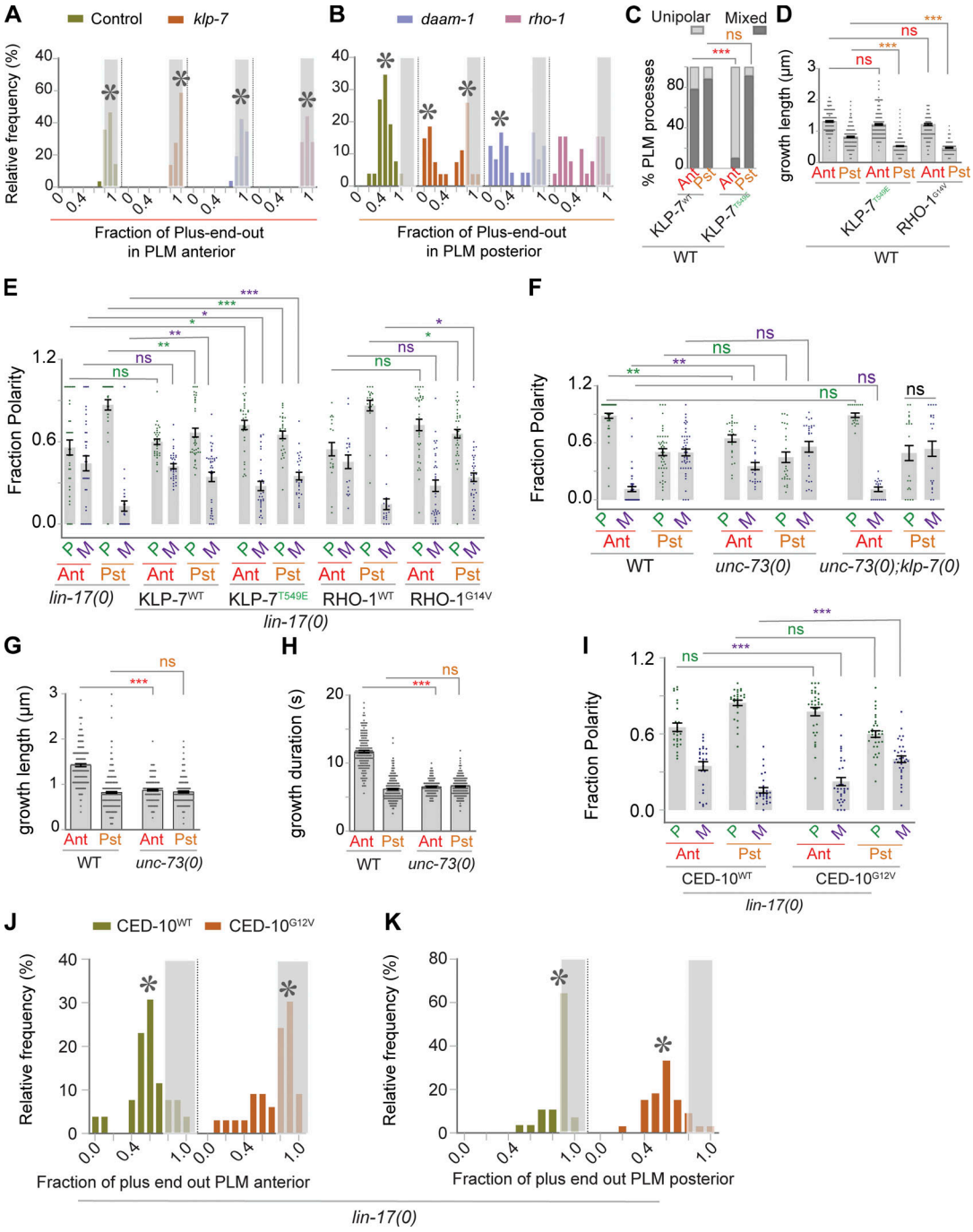

Figure S5. **Regulation of microtubule polarity through Wnt PCP components, related to Fig. 8. (A and B)** Relative frequency distribution of the fraction of microtubules with plus-end-out polarity in anterior (A) and posterior (B) processes due to the RNAi of *klp-7*, *daam-1*, and *rho-1*. Asterisks indicate the mode value for each distribution, and the gray shaded areas cover the population of the microtubules having fraction polarity value 0.8 or above. N = 3–4 independent replicates; *n* (number of neurons) = 23–29. **(C)** Change in the percentage of PLM processes with microtubules oriented either in unipolar (lighter gray) or mixed (darker gray) manner due to expression of KLP-7^{WT} and active version (A-type) of KLP-7 (KLP-7^{T549E}) in WT worms. N = 3 independent replicates; *n* (number of neurons) = 25–31. Ant, anterior; Pst, posterior. **(D)** Growth length of the EBP-2 tracks due to the expression of either an activated version of KLP-7 (KLP-7^{T549E}) or RHO-1^{G14V}. N = 3 independent replicates; *n* (number of tracks) = 170–530. **(E)** The effect on fraction polarity values of microtubules due to the expression of RHO-1^{G14V} or KLP-7^{T549E} in a *lin-17(0)* background. N = 3 independent replicates; *n* (number of neurons) = 20–38. **(F)** The fraction polarity values of microtubules in *unc-73(0)* and *unc-73(0);klp-7(0)* backgrounds. N = 3–4 independent replicates; *n* (number of neurons) = 19–46. **(G and H)** Growth length (G) and duration (H) of the EBP-2 tracks, respectively, in *unc-73(0)*. N = 3–4 independent replicates; *n* (number of tracks) = 170–400. **(I)** The effect on fraction polarity values of microtubules due to the expression of WT (CED-10^{WT}) or activated CED-10 (CED-10^{G12V}). N = 3 independent replicates; *n* (number of neurons) = 28–33. **(J and K)** The change in the frequency distribution of the fraction of microtubules with plus-end-out polarity due to the expression of *Pmec-4*:CED-10^{G12V} in the anterior (J) and posterior (K) processes of PLM in *lin-17(0)*. N = 3 independent replicates; *n* (number of neurons) = 26–33. Datasets were compared by χ^2 (Fisher's exact) test (C) and ANOVA with Tukey's multiple comparison test (D–I). Error bars represent SEM. *, P < 0.05; **, P < 0.01; ***, P < 0.001.

Video 1. **EBP-2::GFP in various genetic backgrounds, related to Figs. 2, 4, and 5.** The time-lapse video shows the events of microtubule growth at the plus ends visualized using the EBP-2::GFP reporter in PLM neurons of various genotypes [WT, *klp-7(0)*, *lin-17(0)*, and *lin-17(0);klp-7(0)*]. EBP-2::GFP comets moving away from the cell body represent plus-end-out microtubules, which are highlighted with green arrows. The comets moving toward the cell body depict minus-end-out microtubules, which are marked with blue arrows. Videos were captured using a spinning disk confocal microscope at a speed of 2.64 frames per second and played at 15 frames per second.

Video 2. **GFP::RAB-3 in various genetic backgrounds, related to Figs. 2, 4, and 5.** The time-lapse video depicts the axonal transport of GFP::RAB-3–labeled synaptic vesicles in the anterograde and retrograde directions in PLM neurons of various genotypes [WT, *klp-7(0)*, *lin-17(0)*, and *lin-17(0);klp-7(0)*]. The anterograde moving particles are marked with green arrowheads, while the retrograde moving particles are marked with magenta arrowheads. The red arrowheads represent the stationary vesicles. Videos were captured using a spinning disk confocal microscope at a speed of 3.19 frames per second and played at 15 frames per second.

Video 3. **Dynamics of the GFP-tagged version of WT KLP-7 and mutant KLP-7$^{S546E\ S555E}$, related to Fig. 9.** The time-lapse video shows the movement of GFP::KLP-7 in PLM neurons of WT, *unc-73(0)*, and *let502* RNAi. Similarly, a GFP-tagged version of the B-type phosphomutant KLP-7$^{S546E\ S555E}$ was also imaged. The movements are indicated by green arrows. Videos were captured using a spinning disk confocal microscope at a speed of 2.64 frames per second and played at 15 frames per second.

Provided online are five tables. Table S1 shows the phenotype in TRNs in mutants affecting microtubule dynamics. Table S2 shows the results of analysis of the number of EBP-2::GFP tracks in various experiments. Table S3 shows the results of analysis of the growth rate of EBP-2::GFP tracks in PLM neurons. Table S4 lists the C. *elegans* strains used in this study. Table S5 lists strains carrying newly generated extrachromosomal transgenes.